Mississippi State University
Scholars Junction

Theses and Dissertations | Theses and Dissertations

11-25-2020

Computational chemistry investigation of gas-phase structures, infrared spectroscopy, and dissociation pathways of isomeric molecules

Widana Kaushalya

Follow this and additional works at: https://scholarsjunction.msstate.edu/td

Recommended Citation

Kaushalya, Widana, "Computational chemistry investigation of gas-phase structures, infrared spectroscopy, and dissociation pathways of isomeric molecules" (2020). *Theses and Dissertations*. 1133.
https://scholarsjunction.msstate.edu/td/1133

This Graduate Thesis - Open Access is brought to you for free and open access by the Theses and Dissertations at Scholars Junction. It has been accepted for inclusion in Theses and Dissertations by an authorized administrator of Scholars Junction. For more information, please contact scholcomm@msstate.libanswers.com.

Computational chemistry investigation of gas-phase structures, infrared spectroscopy, and dissociation pathways of isomeric molecules

By

Widana Kankanamge Dayangani Nirosha Kaushalya

Approved by:

Amanda Patrick (Major Professor)
David O. Wipf
Todd E. Mlsna
Joseph P. Emerson (Graduate Coordinator)
Rick Travis (Dean, College of Arts & Sciences)

A Thesis
Submitted to the Faculty of
Mississippi State University
in Partial Fulfillment of the Requirements
for the Degree of Master of Science
in Chemistry
in the Department of Chemistry

Mississippi State, Mississippi

November 2020

Copyright by

Widana Kankanamge Dayangani Nirosha Kaushalya

2020

Name: Widana Kankanamge Dayangani Nirosha Kaushalya

Date of Degree: November 25, 2020

Institution: Mississippi State University

Major Field: Chemistry

Major Professors: Amanda Patrick

Title of Study: Computational chemistry investigation of gas-phase structures, infrared spectroscopy, and dissociation pathways of isomeric molecules

Pages in Study: 86

Candidate for Degree of Master of Science

While chemical isomers typically have distinct properties, differentiating between them is often an analytical challenge, especially for mass spectrometric methods. Infrared multiple photon dissociation (IRMPD) spectroscopy and ion mobility spectrometry (IMS) can be useful in analysis of such isomeric compounds; however, experimental results alone do not directly provide in-depth structural information. In this thesis, computational chemistry is first used to explain experimental results and understand the conformational preference of the gas phase ions formed from the lithiation of *cis*-3, *cis*-4 and *trans*-4 hydroxyproline isomers and then used in a predictive manner to evaluate IRMPD spectroscopy and IMS as potential paths forward for the characterization of isomeric dye species. Finally, theoretical methods are used to begin to understand the dissociation pathways of lithiated hydroxyproline isomers in the gas phase, which is ongoing.

DEDICATION

I would like to dedicate this master thesis to my husband N. P. Weerasinghe, my parents W.K. Lionel and P.K. Jayalatha, and my sister W. K. D. Jayamini for their love and enormous support.

ACKNOWLEDGEMENTS

This thesis would not be possible without the support and guidance of many wonderful people.

First and foremost, I would like to express my sincere gratitude to my research advisor Dr. Amanda Patrick for her guidance and direction throughout my Master's studies.

To my committee, Dr. David O. Wipf and Dr. Todd E. Mlsna, I am extremely grateful for their assistance and suggestions. I also like to thank my current lab mates: Maleesha De Silva, Baku Acharya and Matthew Carlo who have been friendly, open-minded, and supportive friends.

I would also like to express my gratitude to my family who have given me the strength, love and faith throughout my life.

Lastly, I would like to extend my gratitude to the family of the Chemistry Department at Mississippi State University.

TABLE OF CONTENTS

DEDICATION ii

ACKNOWLEDGEMENTS iii

LIST OF TABLES vi

LIST OF FIGURES vii

CHAPTER

I. INTRODUCTION 1

1.1 Instrumental analysis methods 2
1.1.1 Mass spectrometer 2
1.1.1.2 Electrospray ionization 3
1.1.1.3 Quadrupole ion trap 5
1.1.2 Infrared multiple photon dissociation 7
1.1.2.1 Infrared multiple photon dissociation spectroscopy 8
1.1.2.2 Tunable infrared laser source: FEL 9
1.1.3 Ion mobility spectrometry-mass spectrometry 10
1.2 Computational chemistry 12
1.2.1 Theoretical collision cross section 14

II. INTERPRETATION OF EXPERIMENTAL IRMPD SPECTRA OF PROTONATED AND LITHIATED HYDROXYPROLINE ISOMERS BY DFT CALCULATIONS 16

2.1 Introduction and background 16
2.2 Computational method 18
2.3 Results and discussion 19
2.3.1 Comparison of IRMPD spectra of protonated hydroxyproline isomers with calculated IR spectra 19
2.3.2 Comparison of IRMPD spectra of lithiated hydroxyproline isomers with theoretical spectra 22
2.3.3 Comparison of theoretical infrared spectra of lithiated positional isomers 29
2.4 Conclusion 33

III. THEORETICAL MODELING OF ION MOBILITY SEPARATION AND INFRARED ION SPECTROSCOPY CHARACTERIZATION OF ISOMERIC DYE MOLECULES 35

3.1 Introduction and background....35
3.2 Computational methods....38
3.2.1 Geometry optimization, thermodynamic calculations, and frequency calculations....38
3.2.2 Collision cross section predictions....39
3.3 Results and discussion....39
3.3.1 Indigoid isomers....39
3.3.1.1 Comparison of theoretical infrared spectra of protonated indigoid structural isomers....39
3.3.1.2 Comparison of theoretical IR spectra of sodiated indigoid structural isomers....41
3.3.1.3 Comparison of theoretical infrared spectra of protonated *cis* and *trans* isomers of indigoid isomers....43
3.3.1.4 Comparison of theoretical collision cross sections of protonated indigoid isomers and sodiated indigoid isomers....49
3.3.2 Anthraquinone isomers....51
3.3.2.1 Comparison of theoretical IR spectra of sodiated and lithiated anthraquinone isomers....51
3.3.2.2 Comparison of theoretical collision cross sections of sodiated anthraquinone isomers....55
3.4 Conclusion....56

IV. ONGOING WORK AND CONCLUSIONS....57

4.1 Ongoing work: Understanding the dissociation pathways of lithiated hydroxyproline isomers in the gas phase....57
4.2 Conclusions....57

REFERENCES....59

APPENDIX

A. COORDINATES OF THE LOWEST ENERGY CONFORMERS OF INDIGOID ISOMERS....70

B. COORDINATES OF THE LOWEST ENERGY CONFORMERS OF ANTHRAQUINONE ISOMERS....80

LIST OF TABLES

Table 3.1 Predicted collision cross sections (CCS) for protonated indigo, protonated isoindigo and protonated indirubin.....50

Table 3.2 Predicted collision cross sections (CCS) for sodiated indigo, sodiated isoindigo and sodiated indirubin 50

Table 3.3 Predicted collision cross sections (CCS) for sodiated alizarin, sodiated anthrarufin and sodiated chrysazin.....55

LIST OF FIGURES

Figure 1.1 Basic components of mass spectrometer 3

Figure 1.2 Electrospray ionization process: High voltage is applied to the spraying nozzle. The coulombic repulsion between like charges on the liquid surface lead to come out the meniscus from the capillary. This cause Taylor cone to be generated, from which charged droplets are ejected. The successive solvent evaporation and coulomb fission of these droplets eventually leads to the ejection of bare analyte ions. 4

Figure 1.3 Illustration of the ion evaporation model (IEM) and the charged residue model (CRM) of bare ion formation from charged droplets 5

Figure 1.4 An illustration of a cross-sectional view of a three-dimensional quadrupole ion trap 6

Figure 1.5 Schematic representation of the IRMPD mechanism: The initial absorption of one resonant photon excites the ion from the vibrational ground state to an excited state. This is then followed by IVR, which redistributes the energy into the internal energy of the molecule, allowing for the absorption of another photon of the same resonant energy. This iterative process is continued until the dissociation threshold (D_0) is overcome and fragmentation can occur 8

Figure 1.6 Schematic representation of basic steps in an IRMPD spectroscopy experiment: mass selected ions are irradiated by IR photons of a specific frequency. If the irradiation frequency is resonant with the vibrational mode of the ion, photons are absorbed and IRMPD can occur. If the frequency is not resonant, then the ions do not absorb photons and do not fragment. Mass spectra are recorded as a function of IR frequency and the IRMPD yield is plotted versus wavenumber 9

Figure 1.7 Schematic diagram of main components of free electron laser (FEL) 19

Figure 1.8 Schematic of drift tube ion mobility spectrometry, showing three ion packets consisting of ions of different sizes in the ionization region, which are pulsed into the drift tube, where they move at different velocities through the background gas, allowing for their separation 11

Figure 2.1 (A) salt bridge and (B) charge solvated structure of hydroxyproline.....17

Figure 2.2 Lowest energy conformers of (a) protonated cis-4-hydroxyproline, (b) protonated trans-4-hydroxyproline and (c) protonated cis-4-hydroxyproline. Hydrogen bond lengths, marked by dashed lines, are given in Å 29

Figure 2.3 (A) Theoretical infrared spectrum of the lowest energy conformer and (B) the IRMPD spectrum of protonated *cis*-4-hydroxyproline.....21

Figure 2.4 (A) Theoretical infrared spectrum of the lowest energy conformer and (B) the IRMPD spectrum of protonated *cis*-3-hydroxyproline.....22

Figure 2.5 Lowest-energy conformers found for the charge-solvated form and the salt-bridge form of (A) *cis*-3-hydroxyproline, (B) *cis*-4-hydroxyproline and (C) *trans*-4-hydroxyproline.....23

Figure 2.6 IRMPD spectrum of lithiated *cis*-3-hydroxyproline (A) and theoretical infrared spectra of the most energetically stable charged solvated (B-D) and salt bridge (E-G) conformers with their structures.....24

Figure 2.7 IRMPD spectrum of lithiated *cis*-4-hydroxyproline (A) and theoretical infrared spectra of the most energetically stable charged solvated (B-D) and salt bridge (E-G) conformers with their structures.....26

Figure 2.8 IRMPD spectrum of lithiated *trans*-4-hydroxyproline (A) and theoretical infrared spectra of the most energetically stable salt bridge (B-D) and charged solvated (E-G) conformers with their structures.....28

Figure 2.9 Theoretical infrared spectra of the most stable charge solvation (A) and salt bridge (B) conformers of lithiated *trans*-4-hydroxyproline and charge solvation (C) and salt bridge (D) conformers of lithiated *trans*-3-hydroxyproline 30

Figure 2.10 IRMPD spectrum of lithiated *cis*-3-hydroxyproline (A) and the theoretical infrared spectra of the most stable charge solvation (B) and salt bridge (C) conformers at M062X level with the basis set 6-31++G(d, p) with the structures.....31

Figure 2.11 IRMPD spectrum of lithiated *cis*-4-hydroxyproline (A) and the theoretical infrared spectra of the most stable charge solvation (B) and salt bridge (C) conformers at M062X level with the basis set 6-31++G(d,p) with the structures.....32

Figure 2.12 IRMPD spectrum of lithiated trams-4-hydroxyproline (A) and the theoretical infrared spectra of the most stable charge solvation (B) and salt bridge (C) conformers at M062X level with the basis set 6-31++G(d, p) with the structures.....33

Figure 3.1 Structures of *trans* isomers of (A) indigo, (B) isoindigo and (c) indirubin and *cis* isomers of (D) indigo, (E) isoindigo and (F) indirubin.....37

Figure 3.2 Structures of (A) alizarin, (B) anthrarufin and (C) chryzarin.....38

Figure 3.3 Lowest energy conformers of protonated (A) indigo, (B) isoindigo and (C) indirubin at B3LYP/6-31++G(d,p).....40

Figure 3.4 Theoretical IR spectra of (A) indigo, (B) isoindigo and (C) indirubin at B3LYP/6-31++G(d,p) in fingerprint region.....41

Figure 3.5 Lowest energy conformers of sodiated (A) indigo, (B) isoindigo and (C) indirubin at B3LYP/6-31++G(d,p).....42

Figure 3.6 Theoretical IR spectra of sodiated (A) isoindigo, (B) indirubin and (C) indigo at B3LYP/6-31++G(d,p) in fingerprint region.....43

Figure 3.7 Lowest energy conformers found for the protonated (A) *cis,* (B) *trans* indigo, (C) *cis,* (D) *trans* isoindigo and (E) *cis,* (F) *trans* indirubin.....44

Figure 3.8 Comparison of theoretical infrared spectra of protonated (A) *trans* and (B) *cis* indigo in fingerprint region, protonated (C) *trans* and (D) *cis* indigo in NH/OH stretching region at B3LYP/6-31++G(d,p) level of theory 45

Figure 3.9 Comparison of theoretical infrared spectra of protonated (A) *trans* and (B) *cis* isoindigo in fingerprint region, protonated (C) *trans* and (D) *cis* isoindigo in NH/OH stretching region at B3LYP/6-31++G(d,p) level of theory 47

Figure 3.10 Comparison of theoretical infrared spectra of protonated (A) *trans* and (B) *cis* isoindigo in fingerprint region, protonated (C) *trans* and (D) *cis* isoindigo in NH/OH stretching region at B3LYP/6-31++G(d,p) level of theory 48

Figure 3.11 Lowest energy conformers of (A) sodiated alizarin, (B) sodiated anthrarufin and (C) sodiated chrysazin at B3LYP/6-31+G(d) level of theory.....51

Figure 3.12 Comparison of theoretical infrared spectra of sodiated (A) alizarin, (B) anthrarufin, and (C) chrysazin in fingerprint region, sodiated (D) alizarin, (E) anthrarufin, and (F) chrysazin in NH/OH stretching region at B3LYP/6-31+G(d) level of theory.....52

Figure 3.13 Lowest energy conformers of (A) lithiated alizarin, (B) lithiated anthrarufin and (C) lithiated chrysazin at B3LYP/6-311++G(d,p) level of theory.....53

Figure 3.14 Comparison of theoretical infrared spectra of lithiated (A) alizarin, (B) anthrarufin, and (C) chrysazin in fingerprint region, lithiated (D) alizarin, (E) anthrarufin, and (F) chrysazin in NH/OH stretching region at B3LYP/6-31+G(d) level of theory.....54

CHAPTER I

INTRODUCTION

Mass spectrometry is a powerful chemical analysis tool and has been used increasingly in many different subfields of the biological and chemical sciences.[1, 2] The major advantages include requirement of small quantity of sample and short analysis time. Mass spectrometry measures mass-to-charge ratio of ions. Therefore, using only single-stage mass spectrometry (in cases where fragmentation does not occur during the ionization step) neither structural elucidation of molecules nor differentiation of isomeric species can be obtained.

Tandem mass spectrometry (a technique to break down selected ions into fragments) is an approach toward structural characterization and isomer differentiation. Various ion activation and dissociation techniques, including electron capture dissociation (ECD),[3] electron transfer dissociation (ETD),[4] and collision induced dissociation (CID)[5] within the mass spectrometry have been shown to be useful. While each of these various dissociation methods offer their own strengths, it is sometimes impossible to differentiate closely related isomers by tandem mass spectrometry, specifically if they generate the same fragmentation pathways.[6, 7]

Therefore, it is sometimes beneficial if we can use additional methods where the structural properties of the analyte ions are more directly probed. Infrared multiple photon dissociation (IRMPD) spectroscopy and ion mobility spectrometry (IMS) are two such methods. In IRMPD spectroscopy,[8] absorption of multiple photons leads to dissociation of one or more bonds within an analyte ion (More details will be discussed in the later Section 1.1.2). The

absorption of photons, and therefore the dissociation yield at a given wavenumber, depends on the molecular structures of the ion. So, structural differences in isomers can lead to absorption of IR photons at different wavenumbers (preferably unique to each isomer).

In IMS, isomeric species are separated based on their mobilities through a drift tube, which depends on the collisional cross section of the gaseous ions.[6, 9, 10] The differences in shape between isomeric species can be sufficient to provide drift time resolution by IMS.

Alongside all of these mass spectrometry-based approaches to isomer differentiation, computational chemistry provides complementary information. Given the gas-phase nature of the methods, computational chemistry of isolated (e.g., gas-phase) ions is a useful model. For tandem mass spectrometry, computational chemistry can be used for determining the dissociation pathways and structure of fragment ions. For IRMPD, it has been employed to probe the structure of the gas phase ions as well as the dissociation pathways of the ions.[11] For IMS, computational chemistry is used to predict the CCS and structure of the ions.[6]

1.1 Instrumental analysis methods

1.1.1 Mass spectrometer

The basic components of a mass spectrometer are sample inlet, ionization source, mass analyzer, and the detector (see Figure 1.1).[2] The sample is introduced through the sample inlet. Ions are then produced in the ionization source. This can be accomplished directly in the gas phase or the ions can be introduced into the gas-phase. Once gas-phase ions are generated, they are then introduced into the mass analyzer, where they can be differentiated according to their mass-to-charge ratio (*m/z*). The relative abundance of each ion at each *m/z* is recorded by the detector and the information is read into a data system, where the data can be analyzed and interpreted. The mass analyzer and the detectors are normally held under vacuum conditions

whereas depending on the ionization method, the ionization source may or may not be held under vacuum. As an example, electrospray ionization which is utilized in this study is an atmospheric pressure ionization source.

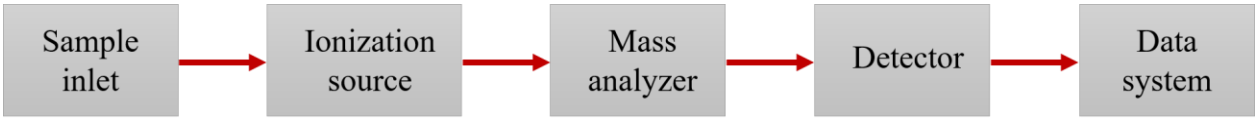

Figure 1.1 Basic components of mass spectrometer

1.1.1.2 Electrospray ionization

Electrospray ionization (ESI)[12, 13, 14] is a soft ionization method. It is useful in analyzing a wide range of analyte ions, including large, nonvolatile ions, so long as the species can be readily charged (e.g., those with fixed charges, acidic sites, basic sites, sites susceptible to metal adduction, etc.). The ESI process generally starts by injecting a dilute solution of analyte to the ESI source by a capillary or a needle at a low flow rate (1–20 μL/min). As seen in Figure 1.2, high voltage (2–3 kV) is applied to a capillary tube with respect to the counter electrode (heated capillary). The applied voltage creates an electric field gradient in the solution phase, which causes to charge separation (positive or negative). The coulombic repulsion between like charges on the liquid surface lead to come out the meniscus from the capillary and deform into a cone, known as "Taylor cone"[15]. After formation of the Taylor cone, it starts to eject a fine jet of liquid from the cone towards the counter electrode. This charged jet can easily breaks down into smaller charged droplets.[13, 16]

Solvent molecules from the emitted charged droplets are evaporated until the Rayleigh limit is reached (where the surface tension of the solution is equal to the coulombic repulsion of

the surface charge), at which point the highly charged droplets are broken down into smaller droplets through the coulomb fission process.[17, 18, 19]

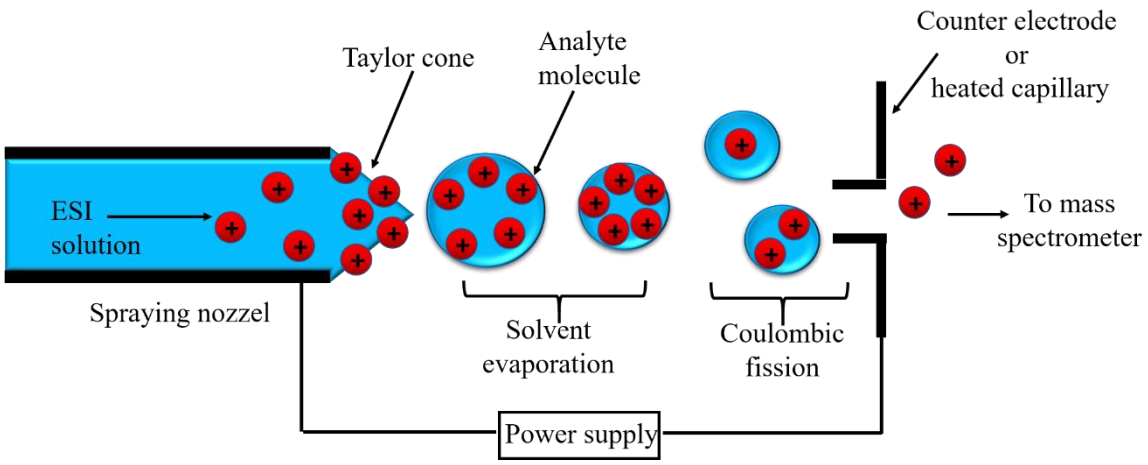

Figure 1.2 Electrospray ionization process: High voltage is applied to the spraying nozzle. The coulombic repulsion between like charges on the liquid surface lead to come out the meniscus from the capillary. This cause Taylor cone to be generated, from which charged droplets are ejected. The successive solvent evaporation and coulomb fission of these droplets eventually leads to the ejection of bare analyte ions.

Gas phase ion formation mechanism from the small charged droplet is still under some debate. However, there are two prevailing mechanisms: the ion evaporation model (IEM)[20] and the charged residue model (CRM).[21, 22] The IEM states that the charged droplet shrink by evaporation until the surface electric field strength is sufficiently large to directly evaporate the bare ions from the surface of the droplet (Figure 1.3). In the CRM, it is assumed that the charged droplet will continue a series of solvent evaporation and coulomb fission until it forms a small charged droplet with only one analyte ion, which finally desolvates to form a bare ion.[18] Evidence suggests that the large macromolecules like proteins follow CRM[23] whereas ion formation of the small molecules follow IEM.[24]

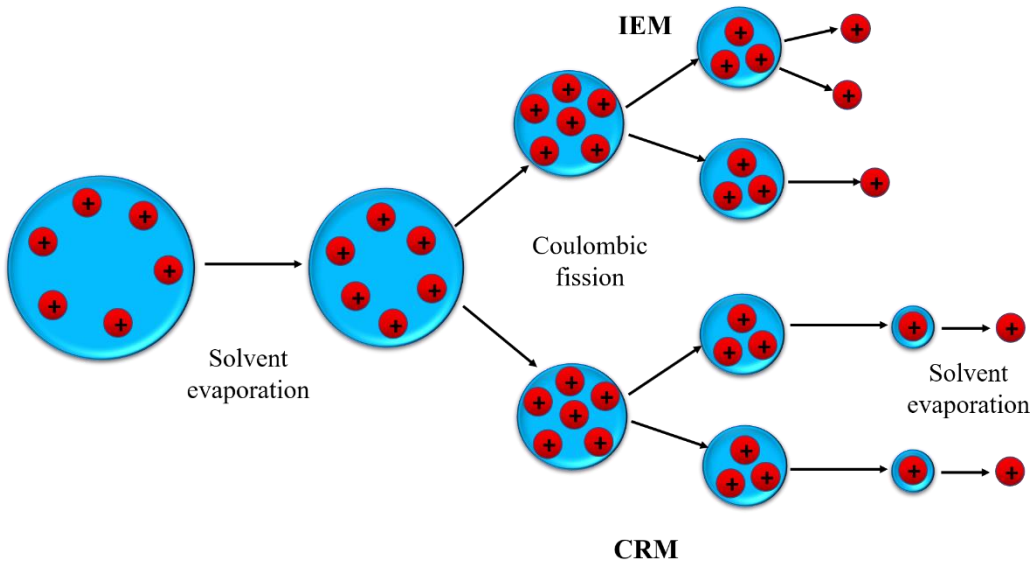

Figure 1.3 Illustration of the ion evaporation model (IEM) and the charged residue model (CRM) of bare ion formation from charged droplets

1.1.1.3 Quadrupole ion trap

In this section, the quadrupole ion trap,[25] will be discussed, as it is the type of mass analyzer with which data presented herein were obtained. Specifically, the data presented in Chapter 2 was measured using a modified quadrupole ion trap mass spectrometer.[26] Here, basic principles of quadrupole ion traps will be discussed.

The three dimensional quadrupole ion trap (3D QIT) consists of three electrodes: a hyperbolic ring electrode and two identical hyperbolic end cap electrodes.[27] Endcap electrodes contain holes to transmit the ions through ion trap, from the source and to the detector. QIT can function as an ion storage device to confine the gaseous ions for a particular period of time (e.g. during irradiation with photons) or as a mass spectrometer to eject mass selectively confined ions

to the detector to measure the *m/z*.[27] For a given radio frequency, ions with a specific *m/z* will have stable trajectories while all the others are unstable. The stable ions can then be ejected from the trap to the detector by ramping the radio frequency.[27] Since QITs can trap ions, select ions with certain *m/z*, activate the ions (during the trapping period) and analyze the mass of the ions all in one location, they can be useful for tandem in time mass spectrometry experiments as well as IRMPD-MS experiment.

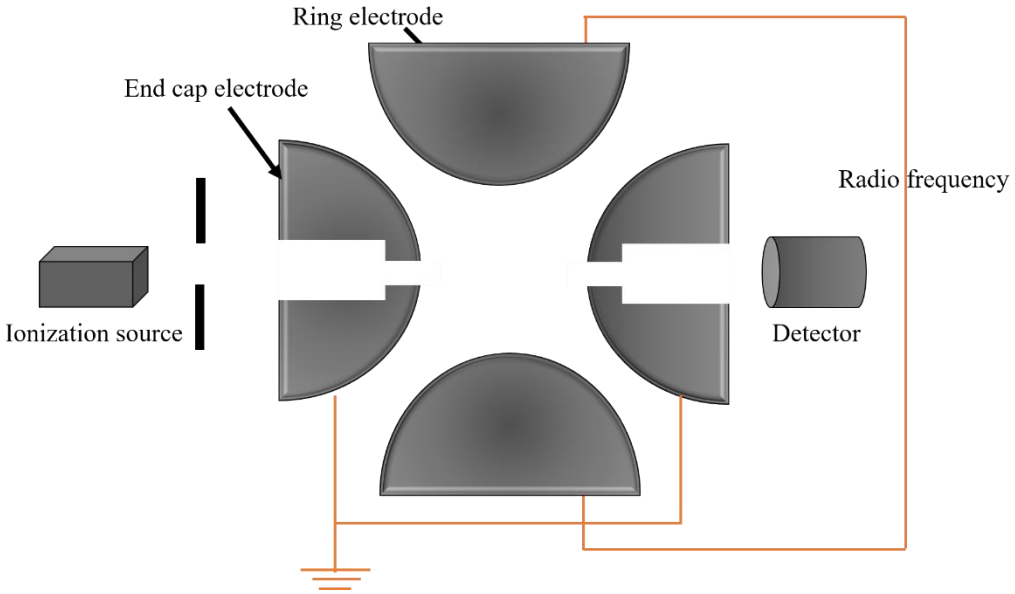

Figure 1.4 An illustration of a cross-sectional view of a three-dimensional quadrupole ion trap

It has been found that the motion of the ions in a QIT can be described mathematically by the solutions to the second order linear differential equation described by Mathieu.[28] The motion of the ions depends on charge and mass of the ions, applied DC and AC voltages and the frequency of the AC voltage. The stability parameters 'a_z' and 'q_z' are used to define the stability of ions in the trap are given by the following equations.[27]

$$a_z = \frac{-8eU}{m\Omega^2 r_0^2} \tag{1.1}$$

$$q_z = \frac{4eV_{RF}}{m\Omega^2 r_0^2} \tag{1.2}$$

Where U is the DC potential, e is charge of the particle, V_{RF} and Ω are the amplitude and the radial frequency of the AC potential, r_0 is the half distance between rods, m is the mass of the ion. The ions can be ejected from the trap when the AC voltage is generated and q value greater than 0.908.[29] As seen in Equation 1.2, q value is depended on the mass and the charge of the ion. So different mass has a unique AC voltage which causes them to exit the trap. Most common mode of the ion operation corresponds to operation on the q_z axis. Because most of the ion trap instrument do not offer the flexibility of applying DC potential to the electrodes, a_z is equal to zero.[27]

1.1.2 Infrared multiple photon dissociation

Infrared multiple photon dissociation (IRMPD)[8, 30] is a method for fragmenting trapped ions in the gas phase. A schematic representation of the IRMPD mechanism is shown in Figure 1.5. When one resonant photon is absorbed by an ion into a specific vibrational mode (v=0), the ion is excited into a higher vibrational level (v=1). Then the energy of that photon is rapidly distributed throughout other vibrational modes of the ion via intramolecular vibration relaxation (IVR).[31] After IVR, the initial absorbing vibrational mode is returned to its ground state and ready to absorb another IR photon with the same frequency. The absorption process is continued until the dissociation threshold (D_0) is overcome, which allows for bond cleavage within the ion.

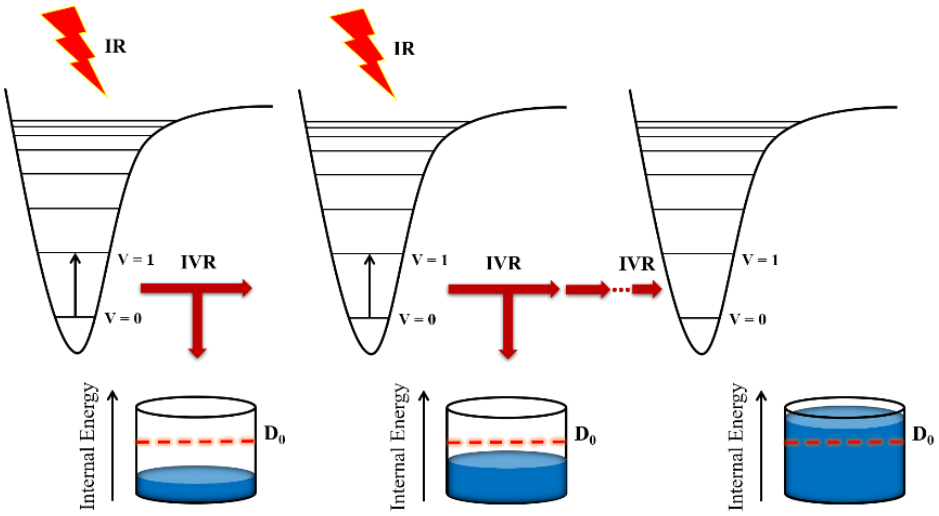

Figure 1.5 Schematic representation of the IRMPD mechanism: The initial absorption of one resonant photon excites the ion from the vibrational ground state to an excited state. This is then followed by IVR, which redistributes the energy into the internal energy of the molecule, allowing for the absorption of another photon of the same resonant energy. This iterative process is continued until the dissociation threshold (D_0) is overcome and fragmentation can occur

1.1.2.1 Infrared multiple photon dissociation spectroscopy

In the IRMPD spectroscopy experiment, the IRMPD yield (Equation 1.3) as a function of irradiation wavenumber is recorded (Figure 1.6). If the irradiation frequency is resonant with a vibrational mode of the ion, then photons are absorbed, and IRMPD occurs. The resulting fragment ions with different *m/z* are then detected by the mass spectrometer (MS).[8] If the irradiation frequency is not resonant with vibrational mode of the ion, the ions do not absorb the photons and dissociation does not occur. To obtain the IRMPD spectrum of an ion for a certain wavenumber range, the experiment has to be repeated at each desired wavenumber step. The resulting IRMPD spectrum is analogous (but not identical) to a more traditional absorption IR spectrum.

$$IRMPD\ Yield = -\ln \frac{I_{Precursor}}{\sum I_{Fragments} + I_{Precursor}} \quad (1.3)$$

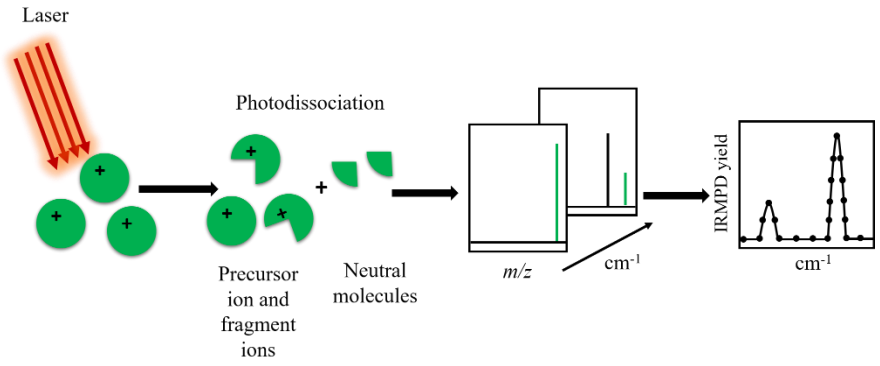

Figure 1.6 Schematic representation of basic steps in an IRMPD spectroscopy experiment: mass selected ions are irradiated by IR photons of a specific frequency. If the irradiation frequency is resonant with the vibrational mode of the ion, photons are absorbed and IRMPD can occur. If the frequency is not resonant, then the ions do not absorb photons and do not fragment. Mass spectra are recorded as a function of IR frequency and the IRMPD yield is plotted versus wavenumber

1.1.2.2 Tunable infrared laser source: FEL

IRMPD spectroscopy experiments have been done using different types of lasers such as CO_2 laser,[32] free electron laser (FEL),[33] and optical parametric oscillator (OPO).[34] These different laser systems produce light in different wavenumber regions. CO_2 laser is operated in the wavelength range 925-1080 cm^{-1}, FEL is operated in 500 – 2000 cm^{-1} (fingerprint region) and OPO is operated in 2000 – 4500 cm^{-1} (NH/OH stretching region).[35] The IRMPD experimental data that I have used in Chapter 2, were collected at a FEL facility. Therefore, in the following section only FEL will be described.

To create FEL, a beam of electrons is produced by the electron gun and accelerated by electron accelerator to relativistic speed (Figure 1.7). As illustrated, the accelerated electron

beam is passed through a periodic magnetic field, called an undulator. Photons are produced due to the transverse acceleration of electrons across the beam path. The wavelength of the emitted radiation can be tuned by changing different factors such as magnetic field strength of the undulators or the energy of the electron beam.[33] In order to achieve tunability in free electron laser for infrared experiments (FELIX), used an undulator with an adjustable gap at fixed electron beam energy.[36]

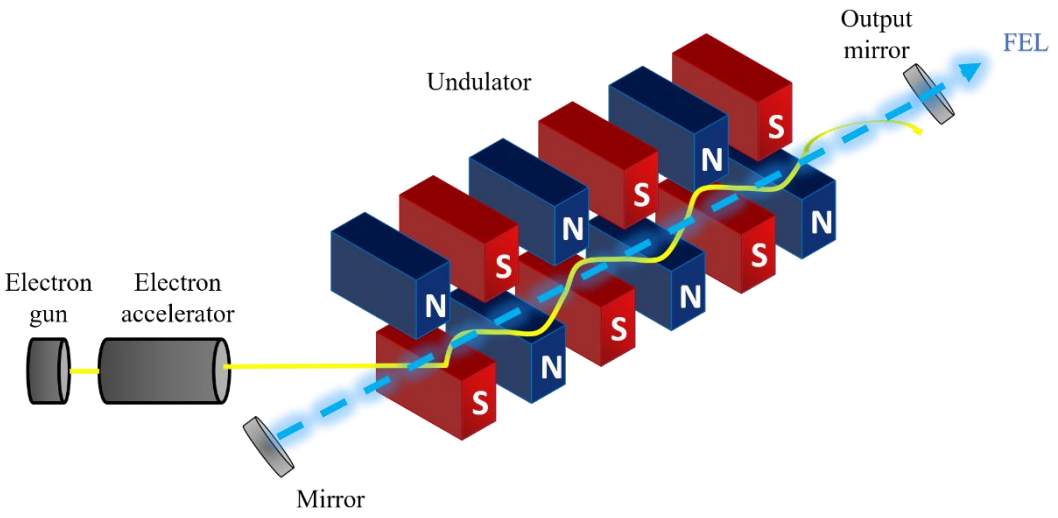

Figure 1.7 Schematic diagram of main components of free electron laser (FEL)

1.1.3 Ion mobility spectrometry-mass spectrometry

In drift tube ion mobility spectrometry (DTIMS),[37] ions move through constant electric field in the presence of neutral gas (usually nitrogen, helium or argon). While travelling through the drift tube, the ions collide with the neutral gas and experience a drag force, impeding their progress toward the detector. Smaller and more compact ions experience fewer collision (less drag), whereas larger and elongated ions experience more collisions (more drag). Thus, firstly

more compact ions reach the detector, followed by less compact/more elongated ions (Figure 1.8).

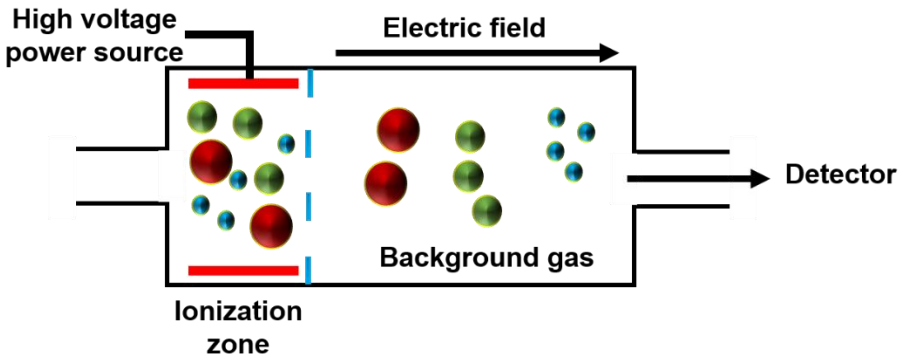

.

Figure 1.8 Schematic of drift tube ion mobility spectrometry, showing three ion packets consisting of ions of different sizes in the ionization region, which are pulsed into the drift tube, where they move at different velocities through the background gas, allowing for their separation

Now, this separation can be considered more mathematically. Ions are separated based on mass, charge, shape, and size.[38,39] The time taken by the ions through the drift tube is recorded. Then using the following Equation 1.4, velocity of the ion can be calculated.

$$V = \frac{L}{t_d} \tag{1.4}$$

Where, V is the velocity, L is the length of the drift tube and t_d is the drift time. If the drift field strength is known (E), the ion mobility of the ion (K) can be determined as follows (Equation 1.5). According to the Equation 1.6, the drift time that an ion needs to pass through the drift region is proportional to the inverse of the mobility.

$$K = \frac{V}{E} \tag{1.5}$$

$$K = \frac{L}{E t_d} \tag{1.6}$$

Mobility of the ion is related to the collision cross section (a reflection of the ion's size/shape) of the ion and, under ideal conditions, can be obtained using Mason-Schamp equation[40] (Equation 1.7).

$$\Omega = \frac{3ez}{16N}\left(\frac{2\pi}{\mu k_b T}\right)^{\frac{1}{2}}\frac{1}{K} \tag{1.7}$$

Where, Ω is the collision cross section, e is the elementary charge, z is the ion charge state, N is the drift-gas number density, μ is the reduced mass of the ion and drift gas, k_B is the Boltzmann constant, and T is the drift-gas temperature.

Isomers have different structural configurations, thus may have different CCS values, in which case can allow for their separation by IMS. Resolution of the isomeric separation can sometimes be increased by several strategies such as varying the drift gas[41] or metal ion adduction.[42, 43] In the present study, CCS of different isomeric molecules of metal adducts were calculated theoretically to predict the trend of the drift time of the isomeric ions in DTIMS.

1.2 Computational chemistry

The aim of the computational calculations in this study is to interpret the measured spectra, to determine thermodynamically preferred ion conformations, to predict theoretical IR spectra, to tentatively predict theoretical CCS values, and to gain mechanistic insights into

dissociation pathways. Calculations include conformational search, structure and energy calculations using quantum chemical method such as density functional theory (DFT), frequency calculations using DFT, and preliminary CCS modeling using Mobcal.[44]

While there are different methods that can be used in computational calculations, all quantum chemistry calculations presented herein were obtained by DFT calculations. DFT was chosen as a compromise between computational speed and theoretical accuracy.[45] DFT methods contains two main parts. The first component is a level of theory to correct for a different degree of electron correlation and the second one is a basis set to describe the molecular orbitals of the system.[46] For modeling systems containing amino acids[47, 48, 49] and dye molecules,[50, 51] it has been found that the hybrid functional of Becke, Lee, Yang and Parr (B3LYP)[52] is well-suited level of theory because it has accurately predicted the experimental results.[50, 49, 53] Additionally, in this present study, hybrid functional M06-2X[54] level of theory was also used for the comparison.

The second component of the DFT method is basis set. The choice of the basis set can greatly affect the accuracy of the calculation. The larger the basis set, the calculations will be more complex. The basis sets used in this study were 6-31++G(d, p) and 6-31+(d). Diffuse functions (denoted by + or ++) are added to improve the accuracy of the results of the molecules having lone pairs. Double plus (++) includes diffuse function on heavy atoms (such as O and N) and lighter atoms (such as hydrogen).[55] Repulsions between electrons can be minimize by adding polarization functions which are denoted by “d” and “p”. In polarization functions, additional orbitals are added, which allow more space for the electrons to get away from each other. Adding polarization functions (d, p) to the basis set result in more accurate computed geometries and vibrational frequencies.

Frequency calculations are performed for optimized geometries, using the harmonic approximation. Scaling factors are applied to the obtained IR frequencies, to compensate for differences between the model and experimental reality. The scaling factor depends on the level of theory and the basis set, and the IR range being studied.[58, 59]

1.2.1 Theoretical collision cross section

Collision cross section (CCS) is a fundamental parameter used to investigate the ion structure in the gas phase by IMS. The theoretical CCS (in three-dimensional model) can be calculated with the help of different theoretical methods. Therefore, accurate CCS calculation methods are vital for the effective application of IMS in structural studies. However, no single method is currently accepted as universally best method for reliably applied for the large range of ions studies in IMS. The choice of the methods used for the calculations are highly variable in literature.[60, 61]

The collision cross section of an ion represents its momentum transfer characteristics during the collisions with the buffer gas molecules. This can be theoretically estimated by the following integral equation (Equation 1.8). In that equation, $\Omega_{avg}^{(1,1)}$ is the averaged collision integral (CCS), θ, φ, and γ angles are described as the collision geometry between the ion and the buffer gas atom, g is the relative velocity, b is the impact parameter, and χ is the scattering angle.[62]

$$\Omega_{avg}^{(1,1)} = \frac{1}{8\pi^2}\int_0^{2\pi} d\theta \int_0^{\pi} d\varphi \sin\varphi \int_0^{2\pi} d\gamma \frac{\pi}{8} \left(\frac{\mu}{k_b T}\right)^3 \int_0^{\infty} dg e^{\frac{-\mu g^2}{2k_b T}} g^5 \int_0^{\infty} db 2b(1-\cos\chi(\theta,\gamma,g,b)) \quad (1.8)$$

In this study, Mobcal software is used to predict the CCS values. This uses three different algorithms; projection approximation (PA), Exact hard sphere scattering (EHSS), and trajectory method (TM).[63] Projection approximation is a simple method for calculating CCSs, which use projection of spherical model atoms to find the orientationally average area of the ions. This method is not considered the scattering effect. PA fails to model momentum transfer between the buffer gas and the molecule. EHSS method consider hard sphere collisions, but disregards long range interactions.[63] In both PA and EHSS calculations, Mobcal program consider the hard-core radius for each atom in the molecular. Because of that the temperature dependence of the collision integral cannot be calculated with these approximations.[64] TM method accounts for both short range and long-range interactions. In addition to that, polarization of the gas molecules by charged analyte molecule is also taken into account.[65]

Kim et al.[44] proposed a modification to the existing trajectory method CCS calculation algorithms for N_2, which takes ion-quadrupole interactions and the orientation of non-spherical gas molecules into account. This modification leads to CCS values that better agrees to the experimentally determined data.[63] In this study, the modified Mobcal program was used to calculates the predicted CCS values of indigoid and anthraquinone isomeric dyes.

CHAPTER II

INTERPRETATION OF EXPERIMENTAL IRMPD SPECTRA OF PROTONATED AND LITHIATED HYDROXYPROLINE ISOMERS BY DFT CALCULATIONS

2.1 Introduction and background

Hydroxyproline is produced by post-translational modification of proline by the enzyme prolyl hydroxylase.[66] Hydroxyproline can exist in isomeric forms such as 4-hydroxyproline or 3-hydroxyproline.[66] These isomeric hydroxyproline have distinct functional roles, which affect the stability and bioactivity of the proteins where they are present. Stability of the triple helical structure is due to the principle form of the collagen, *trans*-4-hydroxyproline.[67] But in type IV, basement membrane collagen, the *trans*-3-hydroxyproline isomer becomes more prominent, involve in the regulation of tendon collagen during the development stage.[68] In addition to that, determination of the level of the hydroxyproline in urine and serum can be useful in diagnosis of several disease**s,**[69] such as thyroid disease and bone disease. Due to the different functions of the hydroxyproline isomers, it is important to differentiate these isomers with a suitable analytical technique.

Ion mobility mass spectrometry (IMS),[6] and infrared multiple photon dissociation (IRMPD) spectroscopy,[7] were used to differentiate hydroxyproline isomers. Previously, a IMS study[6] was performed for *cis*-4-hydroxyproline and *trans*-4-hydroxyproline complexed with alkali metal ions. The computational studies were performed to understand the gas phase chemistry of amino acids with metal cations (conformations of metal adducts).[70, 71] It was found

that stereoisomers (metal adduct *cis* and *trans*) preferred to form two different gas phase conformations for their lowest energy structure. Lithiated *cis*-4-hydroxyproline prefers charged solvated structure whereas *trans*-4-hydroxyproline prefers salt bridge structure.[6]

In previous IRMPD spectroscopy, experimental study together with theoretical calculations showed that protonated *trans*-4-hydroxyproline adopt *exo* configuration and protonated *cis*-4-hydroxyproline adopts *endo* configuration.[7]

Several theoretical studies have been performed to investigate the gas-phase conformations of amino acids upon protonation and metal complexation.[72, 73, 74, 75, 76] Generally, metal ion-complexed amino acids are known to exist in either the charge solvated (CS) or salt-bridge (SB) forms. A CS structure is formed by associating the metal ion with electronegative atoms such as N or O as well as π-clouds in the amino acids. A SB structure is formed by associating the metal ion and deprotonated carboxylic group of amino acid. Figure 2.1 shows the SB and CS structure of hydroxyproline.

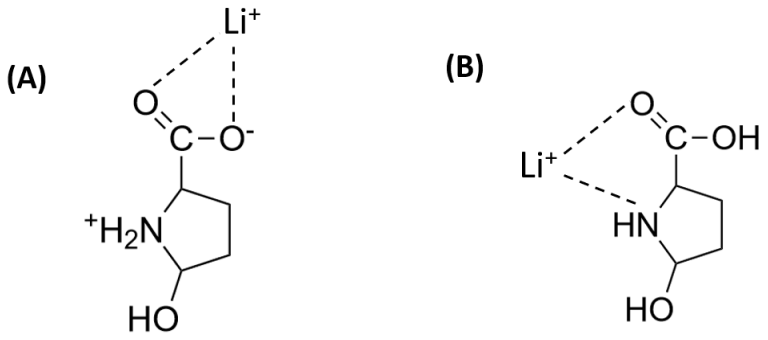

Figure 2.1 (A) salt bridge and (B) charge solvated structure of hydroxyproline

IRMPD spectroscopy turned out to be a useful diagnostic probe to identify SB or CS form of amino acids in the gas phase.[48, 77, 78, 79] Deprotonation of carboxylic group (in SB) and the metal chelation carboxylic group (in CS) absorb infrared photons in different spectral regions. Therefore, carbonyl stretching frequency can be used as the characteristic band to determine CS or SB structure. Comparison of theoretically predicted IR spectra with experimental IRMPD spectra can be helpful in prediction of SB or CS conformation of the ions in the gas phase.[48, 80, 73, 81]

The objective of this study is to perform computational modeling of IR spectra to compare the IRMPD spectra of hydroxyproline isomers, for the purpose of determining the gas phase conformations (SB or CS). The results discussed in this chapter is published.[47]

2.2 Computational method

Experimental measurements presented herein were collected by Dr. Patrick and the FELIX staff in Summer 2019 and have been published.[47] The complementary computational chemistry used to understand these experimental results are described. Computational calculations were performed for the lithium cationized and protonated forms of the relevant hydroxyproline isomers to determine the thermodynamically preferred conformations of each and to facilitate the interpretation of the measured IRMPD spectra.

Starting structures for the lithiated hydroxyproline isomers, *cis*-3-, *cis*-4-, *trans*-3- and *trans*-4 hydroxyproline were drawn according to the conformations shown in the literature.[6] Protonated structures of *cis*-4-hydroxyproline and *cis*-3-hydroxyproline were drawn based on a previous IRMPD spectroscopy study.[7] Then additional conformations were considered by rotating hydroxyl groups and carboxylic group with placing the lithium cation at hydroxyl group, carboxylic acid group, N-atom, and pyrrolidine ring. DFT calculations were carried out using

Gaussian 09 program[82] using B3LYP / 6-31++G(d, p). This level of theory was chosen because it has been shown to produce reliable predictions for a variety of biologically relevant metal adduct complexes in previous works.[6, 83, 84] The theoretical harmonic vibrational frequencies were also calculated. In addition to B3LYP, M06-2X was also used with the same basis to evaluate and validate the efficacy of the computational method. This method was only used for the lithiated hydroxyproline isomers. The coordinates of the lowest energy structures of lithiated *cis*-3-, *cis*-4- and *trans*-4 hydroxyproline are published.[47]

For the comparison of IRMPD spectra, theoretical frequencies were scaled by a factor of 0.975[83] for B3LYP and 0.960[85] for M06-2X level of theory. Theoretical spectra were convoluted using a 10 cm^{-1} full-width-at-half-maximum Gaussian line shape. Avogadro[86] and Gabedit [87] were used for visualization of the computational results.

2.3 Results and discussion

2.3.1 Comparison of IRMPD spectra of protonated hydroxyproline isomers with calculated IR spectra

Figure 2.2 shows the lowest energy conformers found for protonated *cis*-4-hydroxyproline and *trans*-4-hydroxyproline isomers. The lowest energy (calculated at B3LYP / 6-31++G(d,p)) structure of protonated *cis* isomers form endo-conformation whereas lowest energy structure of protonated *trans*-4-hydroxyproline forms exo-conformation. This results were similar with the previous IRMPD study for the hydroxyproline isomers where the lowest energy structures calculated at MP2/6-311+G** level of theory.[7]

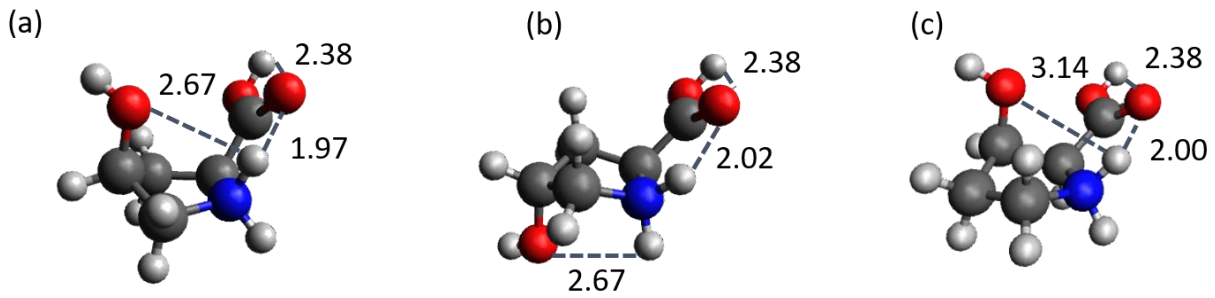

Figure 2.2 Lowest energy conformers of (a) protonated cis-4-hydroxyproline, (b) protonated trans-4-hydroxyproline and (c) protonated cis-4-hydroxyproline. Hydrogen bond lengths, marked by dashed lines, are given in Å

Comparison of the predicted spectrum of the lowest energy conformer along with the experimental IRMPD spectrum for protonated *cis*-4-hydroxyproline can be seen in Figure 2.3. The relative positions of the absorption bands in the IRMPD spectrum and linear infrared spectrum are closely matched. The predicted band for C(O)H bending and C-O stretching at ~1162 cm^{-1}, CH_2 twisting and NH wagging at 1220 cm^{-1}, NH_2 wagging at 1328 cm^{-1} and the pronounced band at 1777 cm^{-1} for C=O stretching are quite close to the experimental bands observed at ~1155 cm^{-1}, 1215 cm^{-1}, 1323 cm^{-1}, 1770 cm^{-1} respectively.

However, the weak absorption band observed for NH_2 scissoring at 1582 cm^{-1} was considerably shifted by 38 cm^{-1} compared to absorption pattern in the calculated spectra (1620 cm^{-1}). In the previous IRMPD study using the MP2/6-311+G** level of theory,[7] the experimental band appears at 1590 cm^{-1} and their calculations predicted the infrared peak at 1598 cm^{-1}. This suggests that the MP2 level of theory better predicts this mode.[7]

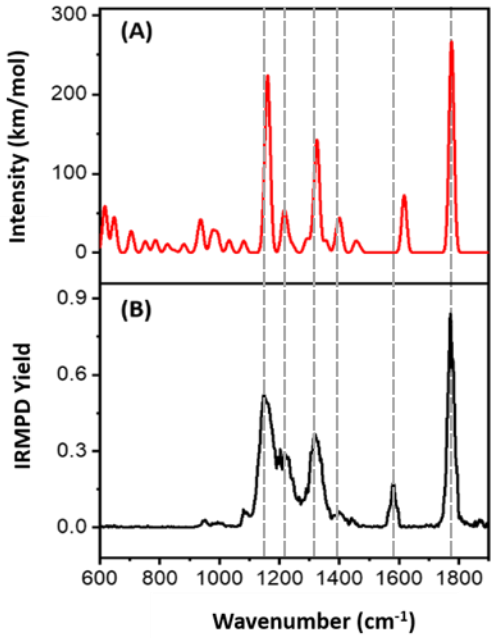

Figure 2.3 (A) Theoretical infrared spectrum of the lowest energy conformer and (B) the IRMPD spectrum of protonated *cis*-4-hydroxyproline

Figure 2.4 shows comparison between the predicted spectrum of the lowest energy conformer and the experimental IRMPD spectrum of protonated *cis*-3-hydroxyproline. Among the active modes for *cis*-3-hydroxyproline, the strong band at 1162 cm^{-1} matched with predicted band at 1160 cm^{-1} for the C-O stretching modes and COH bending mode due to the carboxylic acid group. The broader absorption peak observed in between 1220 -1370 cm^{-1} can be attributed to CH_2 twisting and NH wagging predicted at 1275 cm^{-1} and 1326 cm^{-1}. The strong intense band at 1780 cm^{-1} can be assigned with asymmetric stretching of carbonyl group calculated at 1777 cm^{-1}. Like protonated *cis*-4-hydroxyproline, the weak absorption band was observed at 1584 cm^{-1} for NH_2 scissoring mode which was shifted by 36 cm^{-1} in calculated spectrum.

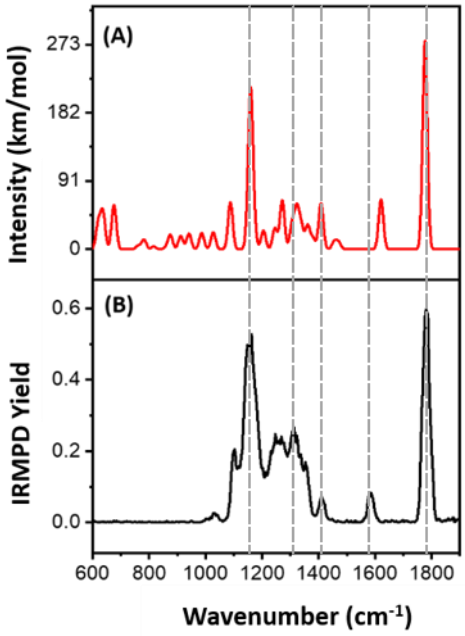

Figure 2.4 (A) Theoretical infrared spectrum of the lowest energy conformer and (B) the IRMPD spectrum of protonated *cis*-3-hydroxyproline

2.3.2 Comparison of IRMPD spectra of lithiated hydroxyproline isomers with theoretical spectra

Figure 2.5 depicts the lowest energy structures found for the lithiated hydroxyproline isomers using the B3LYP functional and the 6-31++(d,p) basis set. Both lithiated *cis*-hydroxyproline isomers form charged solvated (CS) structure whereas lithium adducted *trans*-hydroxyproline forms salt bridge (SB) structure. Similar results were obtained with the previous ion mobility study[6] for the low lying energy structures of stereoisomers of lithiated hydroxyproline with the same level of theory.

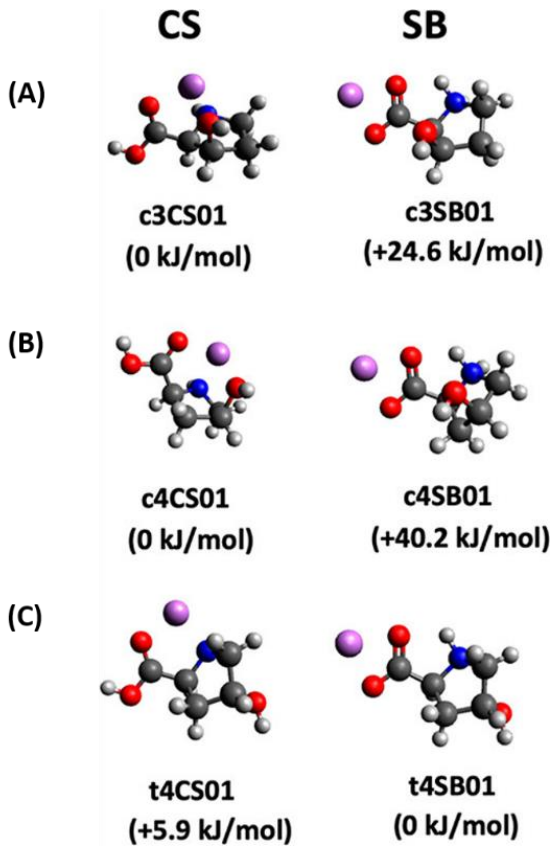

Figure 2.5 Lowest-energy conformers found for the charge-solvated form and the salt-bridge form of (A) *cis*-3-hydroxyproline, (B) *cis*-4-hydroxyproline and (C) *trans*-4-hydroxyproline

Reprinted (adapted) with permission from B. Acharya, W. K. D. N. Kaushalya, J. Martens, G. Berden, J. Oomens, and A. L. Patrick. "A Combined Infrared Ion Spectroscopy and Computational Chemistry Study of Hydroxyproline Isomers". J. Am. Soc. Mass. Spectrom. 2020, 31, 6, 1205-1211. Copyright (2020) American Chemical Society.

Figure 2.6 shows the comparison between the IRMPD spectrum and the infrared spectra of three most stable charged solvated conformations and three most stable salt bridge conformations of lithiated *cis*-3-hydroxyproline. It can be seen that the observed bands are only consistent with the infrared spectrum of the lowest energy conformer of the charged solvated structure (c3CS01).

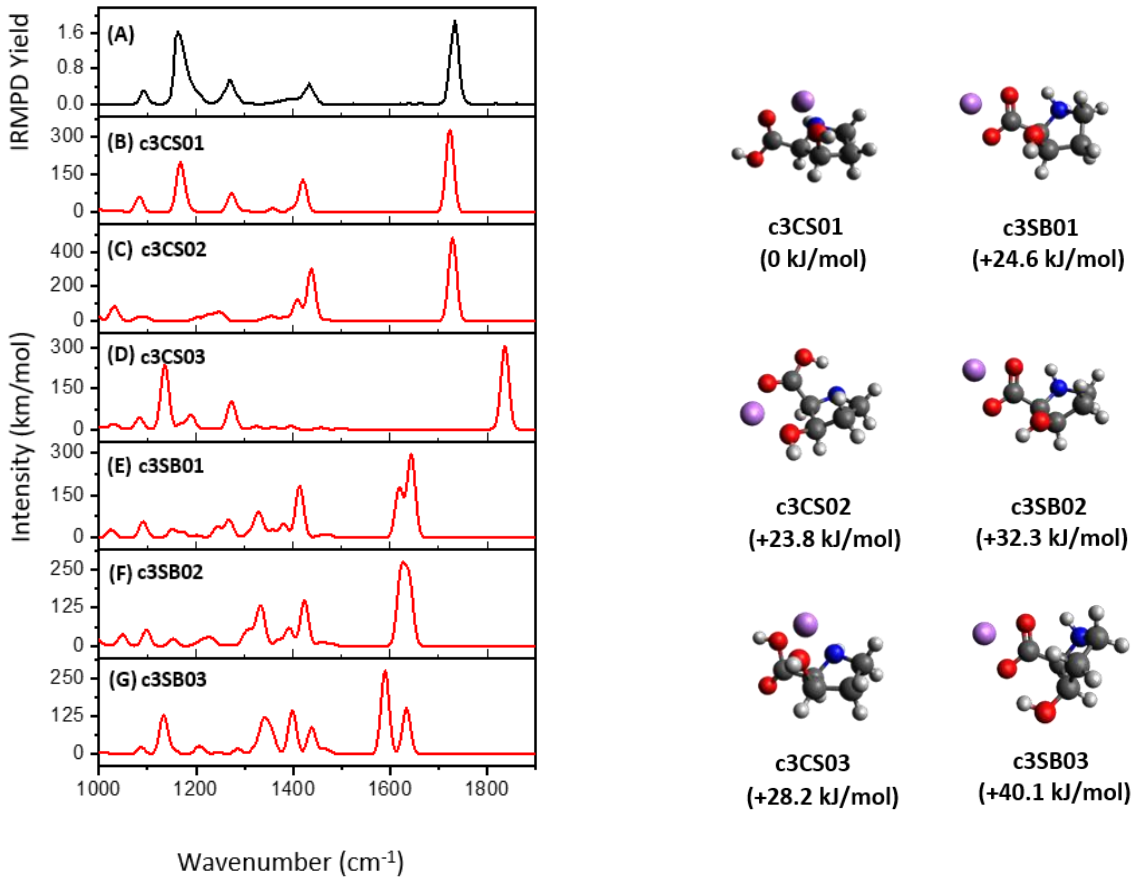

Figure 2.6 IRMPD spectrum of lithiated *cis*-3-hydroxyproline (A) and theoretical infrared spectra of the most energetically stable charged solvated (B-D) and salt bridge (E-G) conformers with their structures

Reprinted (adapted) with permission from B. Acharya, W. K. D. N. Kaushalya, J. Martens, G. Berden, J. Oomens, and A. L. Patrick. "A Combined Infrared Ion Spectroscopy and Computational Chemistry Study of Hydroxyproline Isomers". J. Am. Soc. Mass. Spectrom. 2020, 31, 6, 1205-1211. Copyright (2020) American Chemical Society.

The infrared spectra of both c3CS01 and c3CS02 have two common bands. The strongest peak around 1734 cm^{-1} corresponds to the asymmetric carbonyl stretching, while the second peak corresponds to the C-O stretching at 1423cm^{-1}. The second band is much more intense for c3CS02 than for c3CS01. The c3CS01 spectrum presents another strong band at 1168 cm^{-1} due to the OH bending. In the case of c3CS03, only one common absorption band around 1205 cm^{-1}

can be seen in c3CS01 conformer. The presence of SB conformer can be predicted with the two bands presents in between 1600−1750 cm^{-1}(c3SB01, c3SB02, c3SB03). One band is for NH_2 scissoring and the other for antisymmetric C=O stretching. In all SB theoretical spectra group of peaks exists between 1100 cm^{-1} and 1450 cm^{-1}, which is associated with the C-O stretching and CH_2, CH, and NH_2 bending in SB conformers.

IRMPD spectrum exhibits two strong bands and two weak bands (Figure 2.6 (A)). The strongest peak of IRMPD spectrum shows at 1738 cm^{-1}. It has been found that the all the predicted spectra for the charged solvated conformers shows strongest band above 1700 cm^{-1}, but none of the salt bridge conformer show any bands above 1700 cm^{-1}. The next strong band shows at 1162 cm^{-1}, and two weak bands at 1267 cm^{-1} and 1433 cm^{-1}. Based on this analysis of the relative positions of the experimental and calculated bands, c3CS01 conformer (lowest energy conformer) for lithiated *cis*-3-hydrxyproline is the best for the interpretation of the experimental spectrum. This is consistent with energetic values as well. Because all the other conformers of both charge solvated and salt bridge are higher than 23 kJ/mol in energy.

The comparison between the IRMPD spectrum and the infrared spectra of three most stable charged solvated conformations and three most stable salt bridge conformations of lithiated *cis*-4-hydroxyproline can be seen in Figure 2.7. Most of the absorption bands of the experimental IRMPD spectrum correspond well with calculated spectrum for lowest energy charged solvated structure (c4CS01) compared to the other calculated infrared spectra. This is consistent with

energetic calculations as well. Because all the other higher energy CS conformers and SB conformers are 25 kJ/mol higher in energy.

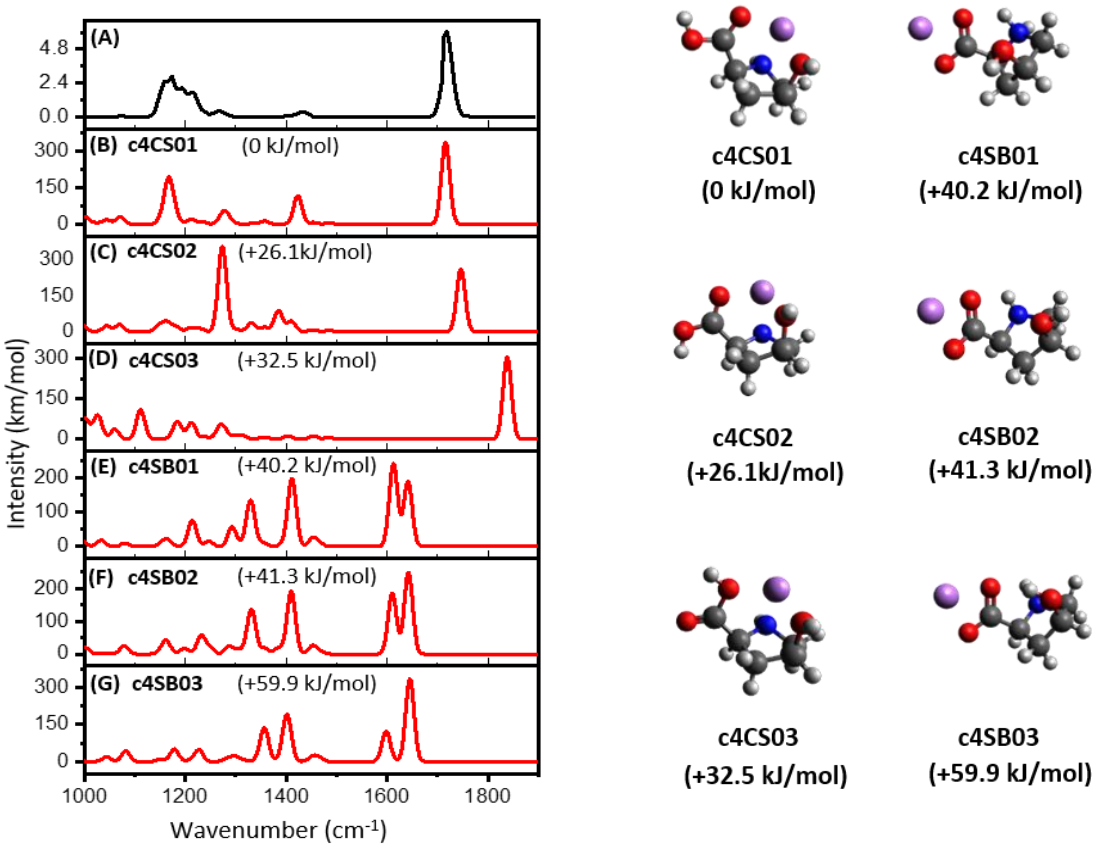

Figure 2.7 IRMPD spectrum of lithiated *cis*-4-hydroxyproline (A) and theoretical infrared spectra of the most energetically stable charged solvated (B-D) and salt bridge (E-G) conformers with their structures

Reprinted (adapted) with permission from B. Acharya, W. K. D. N. Kaushalya, J. Martens, G. Berden, J. Oomens, and A. L. Patrick. "A Combined Infrared Ion Spectroscopy and Computational Chemistry Study of Hydroxyproline Isomers". J. Am. Soc. Mass. Spectrom. 2020, 31, 6, 1205-1211. Copyright (2020) American Chemical Society.

Figure 2.8 shows the comparison between the IRMPD spectrum with calculated spectra of six most stable salt bridge and charged solvated with their structures. The experimental spectrum (Figure 2.8 (A)) exhibits broader band around 1636 cm^{-1}, which corelate well with the expected position of the characteristic C=O stretching mode of the calculated salt bridge (t4SB0 and t4SB02) structures at 1634 cm^{-1}. t4SB01 and t4SB02 are structurally closely related. The energy difference is 1.7 kJ/mol. It can be seen that the both infrared spectra are almost identical and cannot be distinguish experimentally. However, t4SB03 is 15.2 kJ/mol higher in energy. The spectrum of t4SB03 also show some distinguishable bands compared to both t4SB01 and t4SB02 spectra. The weaker band around 1546 cm^{-1} in experiment spectrum, predicted at 1578 cm^{-1} for NH_2 scissoring. The strong band at 1415 cm^{-1} in infrared spectra shows for carbonyl group symmetric stretching, which corresponds to a less intense peak at 1406 cm^{-1} in IRMPD spectrum.

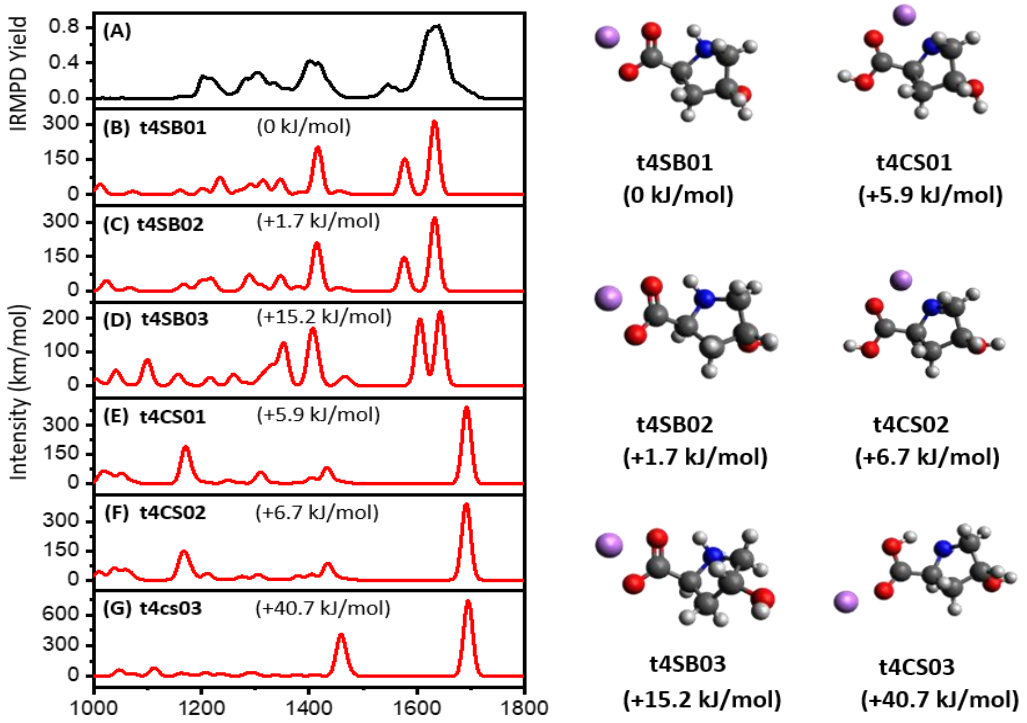

Figure 2.8 IRMPD spectrum of lithiated *trans*-4-hydroxyproline (A) and theoretical infrared spectra of the most energetically stable salt bridge (B-D) and charged solvated (E-G) conformers with their structures

Reprinted (adapted) with permission from B. Acharya, W. K. D. N. Kaushalya, J. Martens, G. Berden, J. Oomens, and A. L. Patrick. "A Combined Infrared Ion Spectroscopy and Computational Chemistry Study of Hydroxyproline Isomers". J. Am. Soc. Mass. Spectrom. 2020, 31, 6, 1205-1211. Copyright (2020) American Chemical Society.

The IRMPD spectrum shows a shoulder peak in the region of the characteristic C=O stretching around 1680 cm^{-1}, which cannot be seen in any salt bridge structure. However, the lowest energy conformers of CS structures (tCS01 and tCS02) show intense band around 1690 cm^{-1}. This suggest there is a minor contribution of the CS conformer in the gas phase. This observation consisted with relative energy values of charged solvated conformer as well. Relative energetic values of two CS conformers, t4CS01 and t4CS02 are +5.9 kJ/mol and +6.7 kJ/mol respectively. Similar results were found with sodiated[88] proline as well.

2.3.3 Comparison of theoretical infrared spectra of lithiated positional isomers

Figure 2.9 shows the theoretical infrared spectra of lowest energy conformer of salt bridge and charged solvated of lithiated *trans*-3-hydroxyproline and lithiated *trans*-4-hydroxyproline. Both isomers energetically favorable to form salt bridge conformer. The charged solvated conformer is 5.9 kJ/mol higher in energy for *trans*-4-hydroxyproline whereas it is 16.6 higher in energy for *trans*-3-hydroxyprloline. The both infrared spectra show three intense bands at 1635 cm^{-1}, 1588 cm^{-1}, and 1410 cm^{-1} for C=O asymmetric stretching, NH_2 scissoring and C=O symmetric stretching respectively. However *trans*-4-hydroxyproline shows an additional strong band at 1333 cm^{-1}, which allows to theoretically differentiate these lithiated positional isomers.

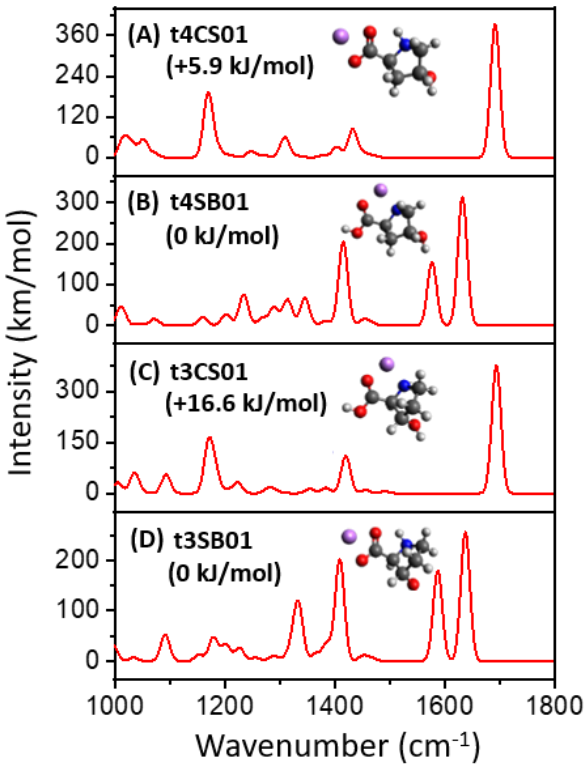

Figure 2.9 Theoretical infrared spectra of the most stable charge solvation (A) and salt bridge (B) conformers of lithiated *trans*-4-hydroxyproline and charge solvation (C) and salt bridge (D) conformers of lithiated *trans*-3-hydroxyproline

Reprinted (adapted) with permission from B. Acharya, W. K. D. N. Kaushalya, J. Martens, G. Berden, J. Oomens, and A. L. Patrick. "A Combined Infrared Ion Spectroscopy and Computational Chemistry Study of Hydroxyproline Isomers". J. Am. Soc. Mass. Spectrom. 2020, 31, 6, 1205-1211. Copyright (2020) American Chemical Society.

Figure 2.10 depicts the comparison between IRMPD spectrum of lithiated *cis*-3-hydroxyproline and the theoretical infrared spectra of the most stable charge solvation and salt bridge conformers at M062X/6-31++G(d,p). Salt bridge conformer lies 47.5 kJ/mol higher energy than the ground state CS conformer for lithiated *cis*-3-hydroxyproline. However, this difference is much higher compared to the energy obtained at the B3LYP level of theory (Figure 2.5). Eventhough the both level of theory predicted CS form as the lowest energy conformer, the

peak position of IR spectrum of CS obtained with M06-2X level of theory much more shifted with the IRMPD than the B3LYP method.

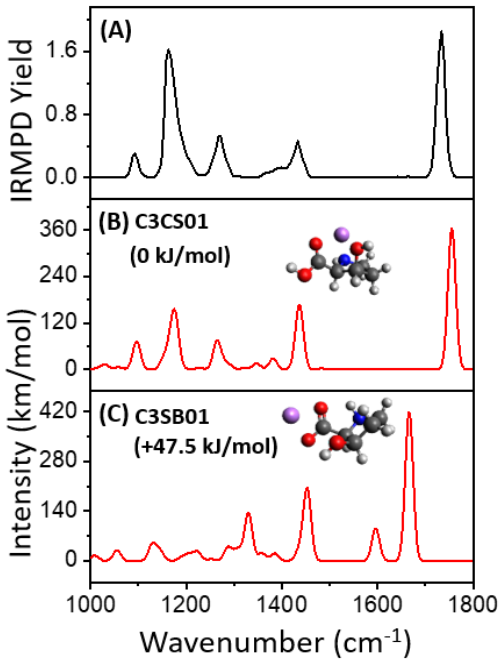

Figure 2.10 IRMPD spectrum of lithiated *cis*-3-hydroxyproline (A) and the theoretical infrared spectra of the most stable charge solvation (B) and salt bridge (C) conformers at M062X level with the basis set 6-31++G(d, p) with the structures.

Reprinted (adapted) with permission from B. Acharya, W. K. D. N. Kaushalya, J. Martens, G. Berden, J. Oomens, and A. L. Patrick. "A Combined Infrared Ion Spectroscopy and Computational Chemistry Study of Hydroxyproline Isomers". J. Am. Soc. Mass. Spectrom. 2020, 31, 6, 1205-1211. Copyright (2020) American Chemical Society.

Figure 2.11 shows the comparison between IRMPD spectrum of lithiated *cis*-4-hydroxyproline and the theoretical infrared spectra of the most stable charge solvation and salt bridge conformers at M062X/6-31++G(d,p). The spectrum pattern obtained for the lowest energy conformer is similar with the infrared spectrum at B3LYP method (Figure 2.7). But experiment bands and the calculated bands position show significant differences.

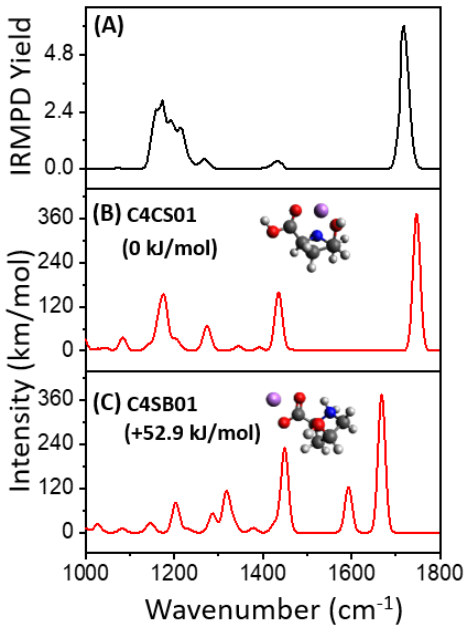

Figure 2.11 IRMPD spectrum of lithiated *cis*-4-hydroxyproline (A) and the theoretical infrared spectra of the most stable charge solvation (B) and salt bridge (C) conformers at M062X level with the basis set 6-31++G(d,p) with the structures.

Reprinted (adapted) with permission from B. Acharya, W. K. D. N. Kaushalya, J. Martens, G. Berden, J. Oomens, and A. L. Patrick. "A Combined Infrared Ion Spectroscopy and Computational Chemistry Study of Hydroxyproline Isomers". J. Am. Soc. Mass. Spectrom. 2020, 31, 6, 1205-1211. Copyright (2020) American Chemical Society.

The lowest energy conformer of *trans*-4-hydroxyproline is CS with M06-2X level of theory as seen in Figure 2.12 (It is SB with B3LYP). However, comparing the experimental spectrum with that infrared spectrum of CS conformer, only the few bands are common in both spectra. When comparing the IRMPD spectrum with the predicted spectrum of SB conformer, some of the bands present in the experimental spectrum can be seen in the infrared spectrum of SB conformer. The energy difference between CS and SB is 3.7 kJ/mol. Therefore, the total experimental spectrum can be a contribution of both predicted spectra of CS and SB conformers.

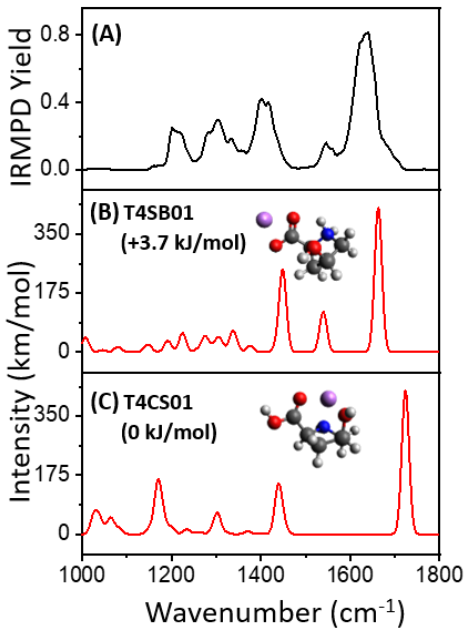

Figure 2.12 IRMPD spectrum of lithiated trams-4-hydroxyproline (A) and the theoretical infrared spectra of the most stable charge solvation (B) and salt bridge (C) conformers at M062X level with the basis set 6-31++G(d, p) with the structures.

Reprinted (adapted) with permission from B. Acharya, W. K. D. N. Kaushalya, J. Martens, G. Berden, J. Oomens, and A. L. Patrick. "A Combined Infrared Ion Spectroscopy and Computational Chemistry Study of Hydroxyproline Isomers". J. Am. Soc. Mass. Spectrom. 2020, 31, 6, 1205-1211. Copyright (2020) American Chemical Society.

2.4 Conclusion

IRMPD spectroscopy together with theoretical calculations have been performed for differentiation of positional and stereoisomers of hydroxyproline molecules. Theoretical calculations with B3LYP method have been shown that the *cis*-4 and *cis*-3-hydroxyproline isomers tend to form charged solvated conformer whereas *trans*-4 and *trans*-3-hydroxyproline form salt bridge structure. When comparing the theoretical spectra of protonated and lithiated isomers, it can be seen that the lithited hydroxyproline isomers show significant difference for both positional and stereoisomers compared to the protonated isomers. Comparing the results

obtained with the other DFT method and M06-2X level of theory, it can be concluded that the B3LYP level of theory is the most suitable method to study the proline type amino acids.

CHAPTER III

THEORETICAL MODELING OF ION MOBILITY SEPARATION AND INFRARED ION SPECTROSCOPY CHARACTERIZATION OF ISOMERIC DYE MOLECULES

3.1 Introduction and background

Natural dyes have been used in textiles and artifacts in the ancient times.[89, 90] Among many, isomers of indigoid (indigo, indirubin, isoindigo)[91, 92] and anthraquinone (alizarin, anthrarufin, chryzarin)[93, 94, 95] and their derivatives were widely used in historical textiles from many thousand years ago. Additionally, those isomers have many other applications. Indigo and its derivatives are used in organic electronic applications.[96] Indirubin and its derivatives are used in cancer treatments.[97] Isoindigo derivatives have been extensively studied as pharmaceuticals,[98, 99] and also used in semiconducting polymers.[96] Anthraquinone isomer, alizarin is commonly used for trace metal extraction and quantification [100, 101] as well as in biochemical studies such as bone growth[102] and tissue engineering.[103] Anthrarufin was utilized as an agent which acts against gram-positive bacteria and also it reduces damaging effects of dioxin.[104] Chryzarin is used in some metal determination.[105]

It is important to analyze the presence of these dyes in historical textiles by which knowledge can be gained in relation to the cultural development. Analysis of dyes are very difficult in historic textiles due to their uniqueness, fragility[106] and low concentration.[89] Chromatographic techniques such as liquid chromatography[107, 108, 109, 110, 111] and gas chromatography [112, 113] have been used to analyze dyes, their isomers and related degradation

products. Tandem mass spectrometry combined with chromatographic techniques was used to differentiate closely related isomeric dyes and their derivatives, if the dissociation pathways of the isomeric ions show diagnostic functions.[114, 115] However, chromatographic techniques have a main drawback which is time consuming. Therefore, it is beneficial to use an appropriate method to differentiate isomers. Two such methods are IRMPD spectroscopy and IMS.

Previously, IRMPD spectroscopy has been used to study protoisomerization (*trans*-to-*cis* isomerization occurs upon protonation) of indigo and isoindigo isomers.[50] In that study, theoretical IR spectra showed two different vibrational frequencies for the C=O stretching mode of *cis* and *trans* isomers. Comparison of IRMPD spectra with theoretical spectra has led to determine the coexistence of the *cis* and *trans* isomers of indigo and isoindigo in the gas phase.[50] Another study has also performed theoretical calculations to show protoisomerization of indigo.[116] Additionally, theoretically computed vibrational frequencies have been used as a guideline to propose the vibrational assignment of the anthraquinone dyes to obtain useful information.[57]

Furthermore, oxazine, which is another type of dyes have also been analyzed by IRMPD spectroscopy with the aid of computational calculations.[51] In this work, four protonated isomers of oxazine dyes (nile red, nile blue a, cresol violet and brilliant cresyl blue) were differentiated. Therefore, it may be beneficial to generate the theoretical IR spectra prior to the experiment to gain the idea about isomers in IRMPD spectroscopy.

Previously, IMS technique has been followed to determine the isomeric distribution of fluorescent laser dye DCM ((4-(Dicyanomethylene)-2-methyl-6-(4-dimethylaminostyryl)-4H-pyran)) in gas phase.[117] Different CCS values were observed for the *cis* and *trans* isomeric forms

of DCM dye. Therefore, theoretical CCS can potentially be used to predict the separation of isomers in IMS study.

The objectives of this study is to predict the possibility of differentiating three indigoid isomers (indigo, isoindigo and indirubin) and their stereoisomers (*cis* and *trans*), and three anthraquinone isomers (alizarin, anthrarufin, chryzarin) with IRMPD spectroscopy and IMS using computational chemistry.

In this study, theoretical IR spectra of indigoid isomers (Figure 3.1) and anthraquinone isomers (Figure 3.2) were evaluated to identify characteristic absorption bands present in each of them. Theoretical CCS were calculated for indigoid isomers and anthraquinone isomers to predict the relative drift time pattern in IMS study.

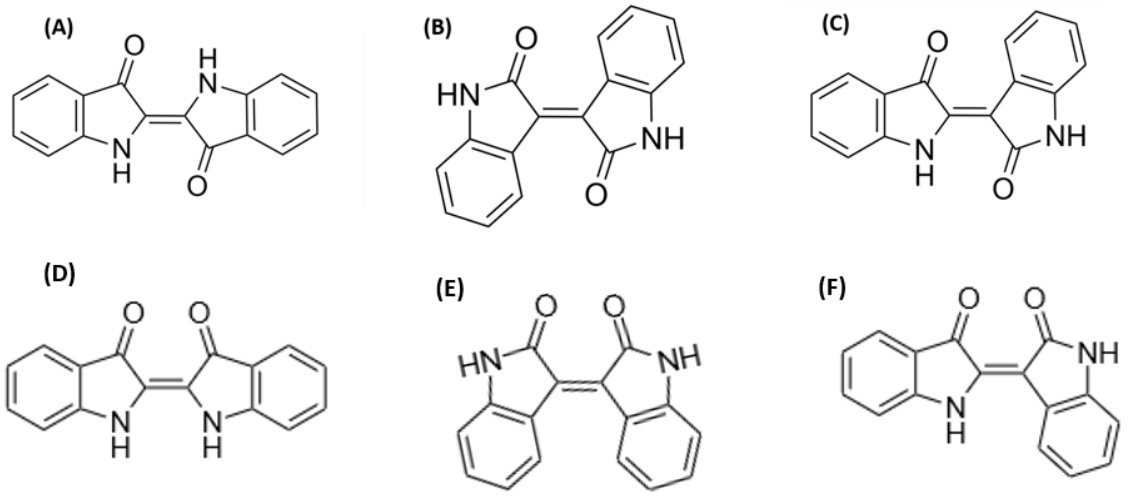

Figure 3.1 Structures of *trans* isomers of (A) indigo, (B) isoindigo and (c) indirubin and *cis* isomers of (D) indigo, (E) isoindigo and (F) indirubin

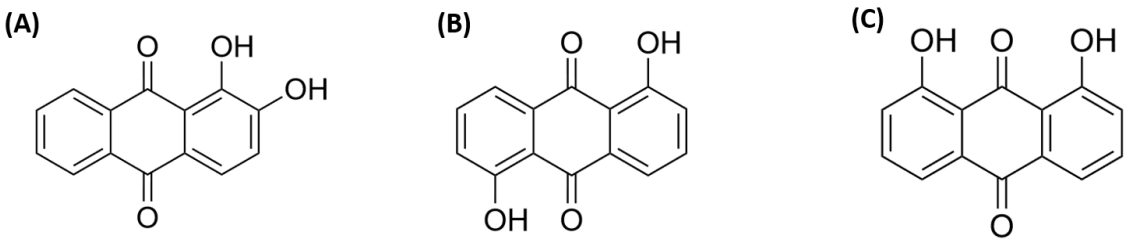

Figure 3.2 Structures of (A) alizarin, (B) anthrarufin and (C) chryzarin

3.2 Computational methods

3.2.1 Geometry optimization, thermodynamic calculations, and frequency calculations

Starting structures for protonated *cis* and *trans* indigo and isoindigo were drawn according to the conformations based on previous IRMPD study.[50] The main sites of protonation were on nitrogen atom and oxygen atom of the carboxylic groups. By binding the proton with preferred binding sites and rotating the OH groups, a wide range of conformations were generated for all the protonated indigoid isomers.

Initial structures of the sodiated alizarin, sodiated anthrarufin, and sodiated chrysazin were generated by binding sodium ion with lone pairs of the two carboxylic acids and lone pairs of two hydroxyl groups, placing the sodium cation with ring systems, and additionally rotating two hydroxyl groups as well. Lithiated conformers of all anthraquinone isomers were generated in a similar way as with the sodium cation.

Indigoid and anthraquinone conformations were generated in the Gabedit software.[118] Quantum mechanics calculations were performed with Gaussian 09 program.[82] Protonated and sodiated indigoid geometries were optimized at the DFT level with B3LYP/6-31++G(d,p).[50] The calculated harmonic frequencies are scaled by a factor of 0.975 [119, 120] below 2000 cm^{-1} and

0.95[121] above 2000 cm^{-1}. Geometry optimization for the sodiated and lithiated anthraquinone conformations were performed with B3LYP/6-31+G(d) level of theory.[57] The same level of theory was used to calculate the theoretical harmonic vibrational frequencies that used to predict the linear infrared absorption spectrum. The calculated frequencies are scaled by a factor of 0.973[122] below 2000 cm^{-1} and 0.961[123] above 2000 cm^{-1}. Calculated vibrational frequencies did not show any imaginary value, indicating that the structures obtained for all isomers were minima. The predicted infrared spectra were convoluted using a 10 cm^{-1} full-width-at-half-maximum Gaussian line shape. Avogadro were used for the visualization of computational results.[86]

3.2.2 Collision cross section predictions

Theoretical collision cross sections calculations were performed for the lowest energy conformers of protonated indigoid isomers and sodiated isomers obtained at B3LYP/6-31++G(d,p) level of theory and sodiated anthraquinone isomers at B3LYP/6-31+G(d) level of theory. Calculations were carried out with the trajectory method implemented in the MobCal-N_2 program[44] at 298K.

3.3 Results and discussion

3.3.1 Indigoid isomers

3.3.1.1 Comparison of theoretical infrared spectra of protonated indigoid structural isomers

Neutral forms of indigo, isoindigo and indirubin have planer structures. The lowest energy conformers of protonated indigo, isoindigo, and indirubin are shown in the Figure 3.3. According to that, upon the protonation, indigo does not change its planer structure. However, protonated isoindgo and indirubin force the conjugated system to twist out of plane.

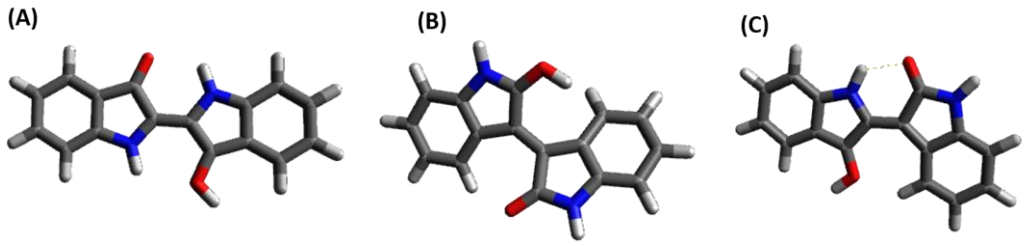

Figure 3.3 Lowest energy conformers of protonated (A) indigo, (B) isoindigo and (C) indirubin at B3LYP/6-31++G(d,p)

Figure 3.4 shows the comparison of the theoretical IR spectra of structural indigoid isomers (*trans*-isomers). In the corresponding spectra, C=O stretching predicted at 1773 cm^{-1} for protonated indigo, 1804 cm^{-1} for protonated isoindigo and 1782 cm^{-1} for protonated indirubin. In the spectrum of protonated indigo, the band with the highest intensity at 1680 cm^{-1} is for the C=C stretching mode at the center of the molecule. The protonated spectra of isoindigo and indirubin show highest intense bands for C=C stretching mode of the benzene rings at 1668 cm^{-1} and 1671 cm^{-1} respectively. The corresponding peak is predicted at 1628 cm^{-1} for protonated indigo. Because of those significant differences, C=O stretching mode and C=C stretching mode of the benzene ring can be used as characteristic bands for differentiating these isomers theoretically in the fingerprint region. IRMPD spectroscopy experiments can be carried out for further investigation of these protonated structural isomers. Moreover, the spectra of sodiated indigoid isomers were also predicted to explore further differences.

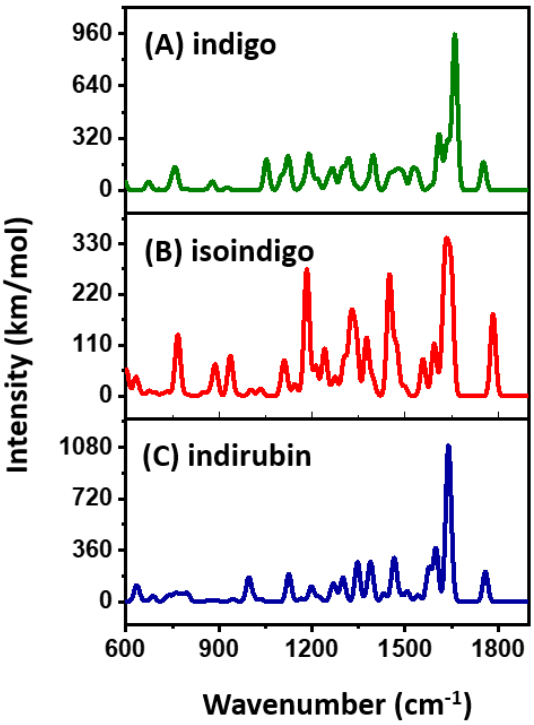

Figure 3.4 Theoretical IR spectra of (A) indigo, (B) isoindigo and (C) indirubin at B3LYP/6-31++G(d,p) in fingerprint region

3.3.1.2 Comparison of theoretical IR spectra of sodiated indigoid structural isomers

Figure 3.5 depicts the lowest energy conformers of sodiated indigo, isoindigo and indirubin. Sodium cation can interact with electronegative atoms such as N and O present in the indigoid isomers. Those interactions can change the conformations of isomeric structures. However, upon the sodiation, the conjugated systems of isoindigo and indirubin are forced to twist out of the plane.

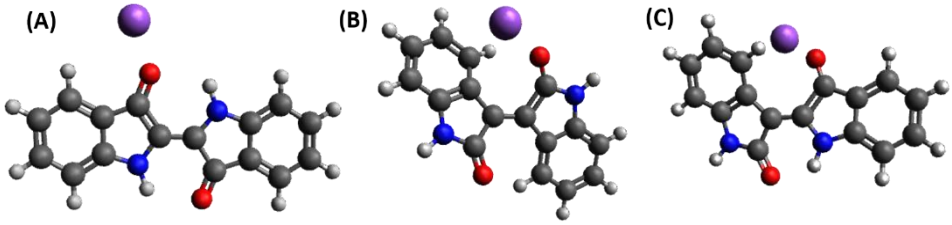

Figure 3.5 Lowest energy conformers of sodiated (A) indigo, (B) isoindigo and (C) indirubin at B3LYP/6-31++G(d,p)

Theoretical IR spectra of sodiated indigoid isomers in fingerprint region is shown in Figure 3.6. Theoretical spectrum of indigo shows one band for C=O stretching at 1729 cm^{-1}. Sodiated indirubin shows two distinct bands for the two different C=O groups which are predicted at 1725 cm^{-1} and 1626 cm^{-1}. Spectrum of sodiated isoindigo also shows two absorption bands for C=O stretching modes. The highest intense band is at 1677 cm^{-1} for vibration mode of C=O group which is interacted with sodium atom. The other band is at 1750 cm^{-1} for vibration mode of C=O group which is far away from the sodium atom. Spectra of sodiated indigo and indirubin show highest intense bands at 1548 cm^{-1} and 1609 cm^{-1} for C=C stretching mode of the ring system respectively. According to the remarkable differences in wavenumbers of C=O stretching mode of sodiated isomers, it can be used as a characteristic band to theoretically differentiate those three sodiated isomers in fingerprint region.

When compare spectra of protonated and sodiated isomers, spectra of protonated indigoid isomers predict one band for C=O stretching mode for each isomer, whereas spectra of sodiated indirubin and isoindigo show two bands for two different C=O stretching modes. So, for further clarifications, IRMPD spectroscopy experiments can be carried out for these sodiated structural isomers.

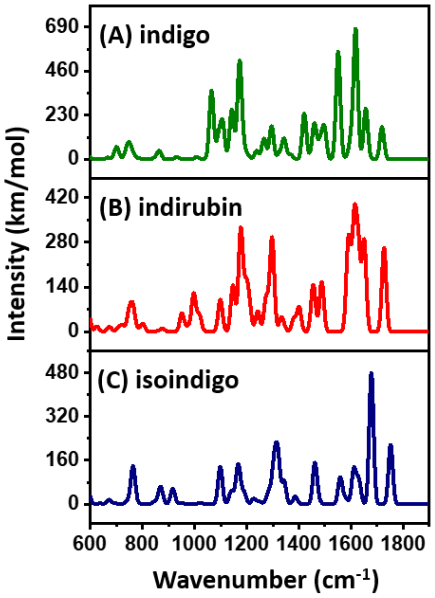

Figure 3.6 Theoretical IR spectra of sodiated (A) isoindigo, (B) indirubin and (C) indigo at B3LYP/6-31++G(d,p) in fingerprint region

3.3.1.3 Comparison of theoretical infrared spectra of protonated *cis* and *trans* isomers of indigoid isomers

Protoisomerization of indigoid dyes, its isomers and derivatives have been investigated both experimentally and theoretically.[50, 116, 124] In the present study, IR spectra of *cis* and t*rans* forms of each indigoid isomer was presented in both fingerprint and NH/OH stretching region. All the indigoid isomers have two possible protonation sites: NH nitrogen and C=O oxygen. But all N-protonated conformers have higher energies compared to O-protonated conformers. Similar results were obtained in previous studies as well.[50, 116] O-protonated conformers may be more favorable in gas phase because of the presence of high degree of conjugations in these isomeric dye systems which leads to resonance stabilization of partially charged O site after the protonation. Therefore, further theoretical studies have been done with the lowest energy

conformers of each O-protonated isomer. Figure 3.7 depicts the lowest energy structures found for each protonated (O site) indigoid isomer (*cis* and *trans*) at the B3LYP/6-31++G(d,p) level of theory. According to the calculations, protonated *trans* indigo is +11.22 kJ/mol higher in energy than its *cis* isomer. The energy difference between *cis* and *trans* isomers of isoindigo and indirubin are 66.81 kJ/mol and 60.31kJ/mol respectively.

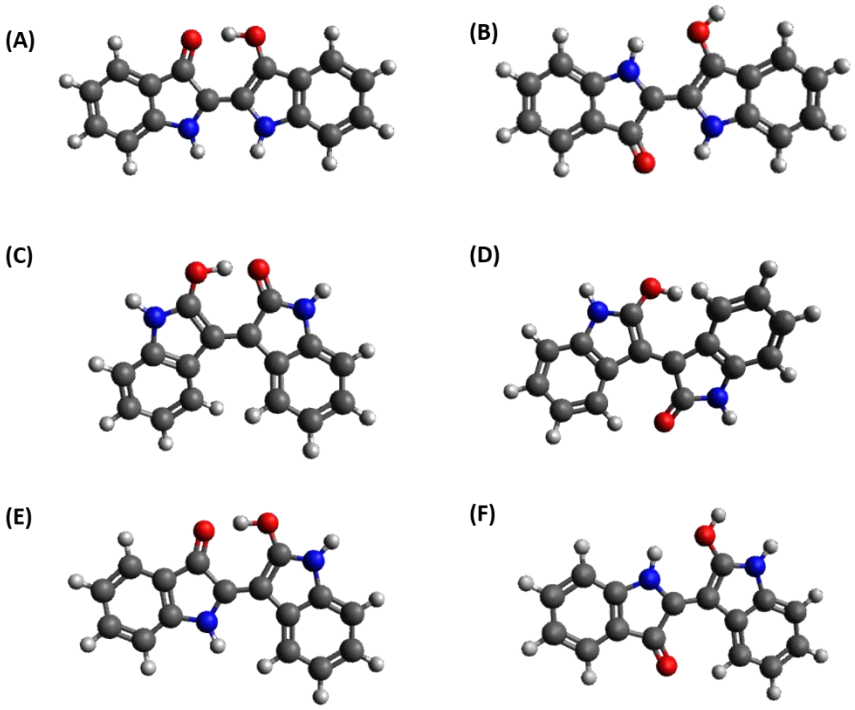

Figure 3.7 Lowest energy conformers found for the protonated (A) *cis*, (B) *trans* indigo, (C) *cis*, (D) *trans* isoindigo and (E) *cis*, (F) *trans* indirubin

Figure 3.8 shows the comparison between the theoretical infrared spectra of most stable protonated *cis* and *trans* indigo isomers in fingerprint region and NH/OH stretching region. The IR spectrum of *cis*-indigo [1] (Figure 3.8(A)). shows absorption band at around 1734 cm^{-1} for

C=O stretching and *trans*-indigo predicts stretching vibration of unprotonated carbonyl group that is hydrogen bonded with the neighboring NH group at around 1671 cm^{-1} (Figure 3.8(B)). Previous IRMPD study, predicted the C=O stretching for *cis*-indigo at 1675 cm^{-1} and *trans*-indigo at 1733 cm^{-1}.[50] Therefore, the position of the C=O stretching frequency in theoretical IR spectra of *cis/trans* structure could be useful as a characteristic band.

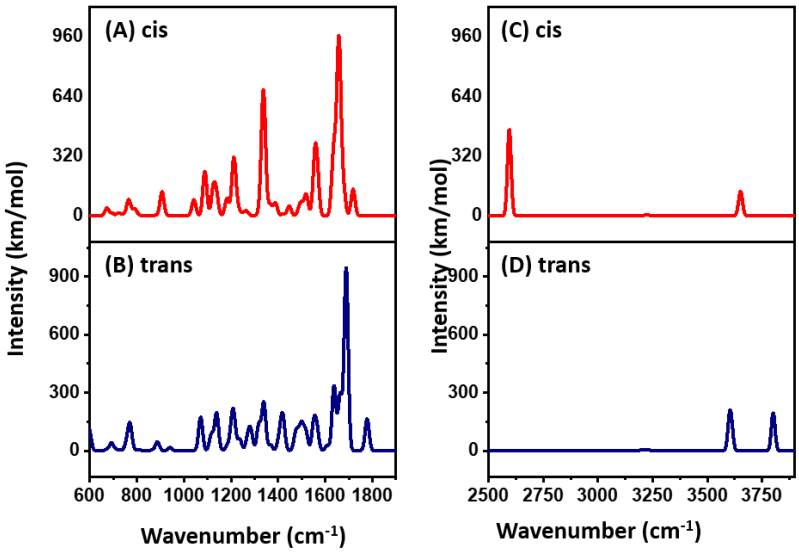

Figure 3.8 Comparison of theoretical infrared spectra of protonated (A) *trans* and (B) *cis* indigo in fingerprint region, protonated (C) *trans* and (D) *cis* indigo in NH/OH stretching region at B3LYP/6-31++G(d,p) level of theory

The dominant band for both *cis*- and *trans*-indigo is the vibrational mode of C=C stretching of the central CC bond between the ring systems, predicted at 1616 cm^{-1} and 1646 cm^{-1} respectively. The second most intense band for the protonated *cis*-indigo shows absorption at 1305 cm^{-1} which is due to combined CH and NH bending modes. *trans*-indigo also shows a peak at around 1307 cm^{-1} for the same vibrational modes with very low intensity. Additionally,

the spectrum of *trans*-indigo predicted an absorption band at 1381 cm^{-1} for ring vibrations coupled with NH and CH in plane bending, which was 1378 cm^{-1} in a previous IRMPD study.[50] The absorption band calculated at 1247 cm^{-1} for the ring vibrational character of the *trans*-indigo.

IR spectra for NH/OH region has not been reported in the previous IRMPD study.[50] In NH/OH stretching region, the strongest calculated peak shows 2526 cm^{-1} for OH stretching mode for *cis*-indigo (Figure 3.8 (C)). However, the predicted absorption of OH stretching mode for *trans*-indigo (Figure 3.8 (D)) blue shifted to a higher wavenumber (3705 cm^{-1}).The significant difference in wavenumber is due to the formation of intermolecular H bonding between OH group and the C=O group in *cis*-indigo, which tend to form stable resonance structure of 6-membered ring. NH stretching vibration can be seen at 3559 cm^{-1} and 3514 cm^{-1} for *cis* and *trans* indigo respectively. The red shift of predicted value of *trans* indigo is because of the formation of H bond of NH group with the neighboring OH group. These two characteristic bands allow to differentiate *cis*- and *trans*-indigo isomers in NH/OH stretching region theoretically.

The comparison of theoretical infrared spectra of protonated *trans* and *cis* isoindigo in fingerprint region and NH/OH stretching regions are shown in Figure 3.9. The theoretical spectrum of *cis*-isoindigo includes a band for C=O asymmetric stretch at 1701 cm^{-1}; whereas the same mode for *trans*-isoindigo is predicted at 1790 cm^{-1}. The difference in the C=O stretch can be used as a characteristic band for the identification of presence of *cis* and *trans* isoindigo in gas phase. Additionally, a unique absorption band calculated at around 1889 cm^{-1} for OH stretching of *cis*-isoindigo due to the formation of hydrogen bond[125] (Figure 3.7 (C)). The most intense band predicted at 1419 cm^{-1} for *cis*-isoindigo contributes to ring stretching and in-plane CH

bending character. *trans*-isoindigo depicts absorption band around 1675 $cm^{-1}$for NH bending mode. The presence of distinct bands in both isomers allows the differentiation of them in fingerprint region theoretically.

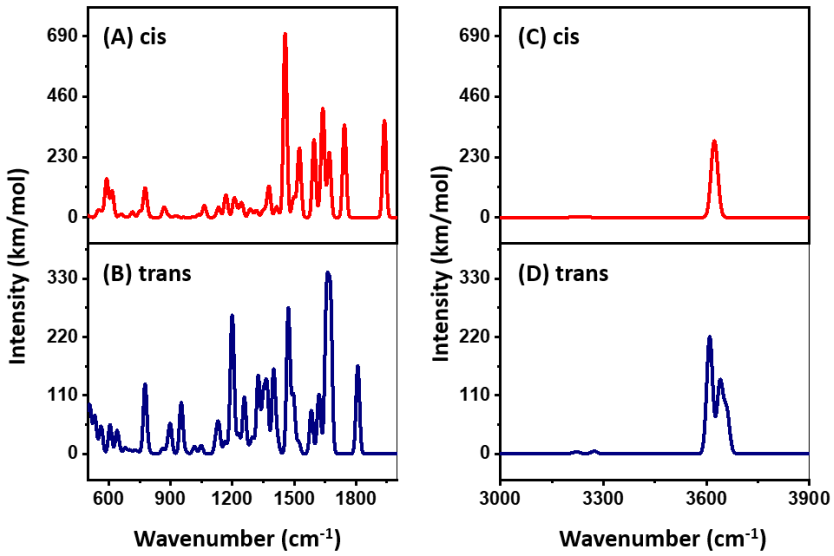

Figure 3.9 Comparison of theoretical infrared spectra of protonated (A) *trans* and (B) *cis* isoindigo in fingerprint region, protonated (C) *trans* and (D) *cis* isoindigo in NH/OH stretching region at B3LYP/6-31++G(d,p) level of theory

In NH/OH stretching region, theoretical spectrum of *cis*-isoindigo (Figure 3.9 (C)) shows one peak in higher wavelength (3532 cm^{-1}) for NH stretching vibration mode. *trans*-isoindigo (Figure 3.9 (D)) shows two bands at around 3519 cm^{-1} and 3552 cm^{-1} for the same vibrational mode. Those calculations show that the region between 3000 cm^{-1} – 4000 cm^{-1} is more useful in identification of *cis/trans* isomers theoretically.

The theoretical infrared spectra of protonated isomers of indirubin in fingerprint and NH/OH stretching regions are shown in Figure 3.10. In the spectra, the strongest band for *trans*-

indirubin can be seen at 1586 cm^{-1} for both ring stretching and NH bending, and the corresponding peak (at 1465 cm^{-1}) of *cis*-indirubin is predicted at a very low intensity. Two distinct bands were obtained at 1625 cm^{-1} and 1687 cm^{-1} for C=O stretching of *cis*-indirubin and *trans*-indirubin respectively. The characteristic C=O band and other distinct bands present in the theoretical spectra of the *cis*-indirubin and *trans*-indirubin are promising for the differentiation of the two isomers.

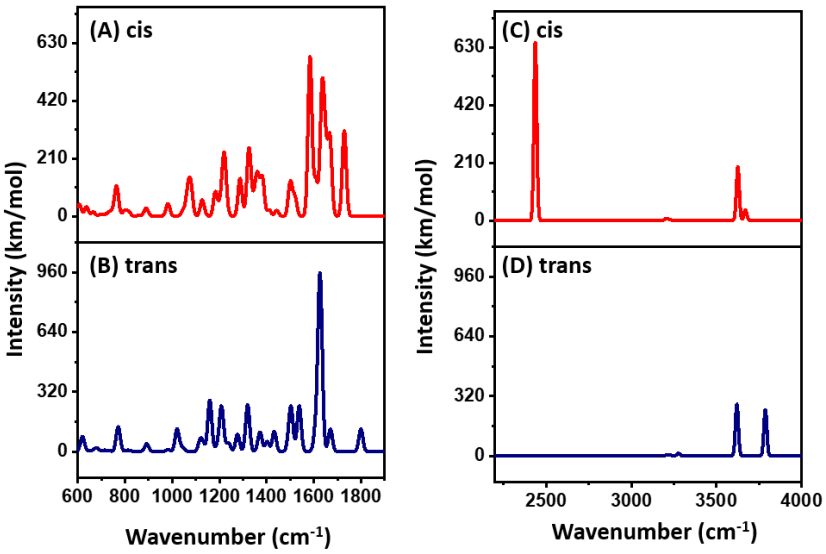

Figure 3.10 Comparison of theoretical infrared spectra of protonated (A) *trans* and (B) *cis* isoindigo in fingerprint region, protonated (C) *trans* and (D) *cis* isoindigo in NH/OH stretching region at B3LYP/6-31++G(d,p) level of theory

Protonated *cis*-indirubin shows a strong absorption band at around 2375 cm^{-1} which can be attributed to the OH stretch. However, the OH stretch of *trans*-indirubin shows at 3786 cm^{-1}. The significant difference in OH stretch in *cis*-indirubin and *trans*-indirubin is due to presence of hydrogen bond between OH and C=O group in c*is*-indirubin. Protonated *ciss*-indirubin shows

two absorption bands at 3534 cm^{-1} and 3579 cm^{-1} for NH stretch whereas *trans*-indirubin shows two bands around 3531 cm^{-1} and 3620 cm^{-1}. Presence of these distinct bands can be useful in distinguishing these two isomers in NH/OH region theoretically.

Previously IRMPD spectroscopy experiment was not carried out to study the protoisomerization of indirubin in gas phase. Therefore, IRMPD experiment can be carried out either in fingerprint region or NH/OH stretching region to investigate whether the protoisomerization of indirubin occurs upon protonation. By comparing the above theoretical spectra with experimental spectra, the coexistence of *cis* and *trans* indirubin can be investigated. Additionally, to estimate the extent of isomerization on-resonance kinetics can be measured on diagnostic and common vibrational frequencies to determine the ratio of *cis*-to-*trans* isomers.

3.3.1.4 Comparison of theoretical collision cross sections of protonated indigoid isomers and sodiated indigoid isomers

Table 3.1 presents the calculated CCS values of lowest energy conformers of protonated *cis*- and *trans*-indigoid obtained at B3LYP/6-31++G(d,p) level theory. All the calculations were performed at 298 K with the trajectory method using nitrogen as the buffer gas. Calculated CCS values for protonated *cis*- and *trans*-indigo are 138.79 $Å^2$ and 136.50 $Å^2$ respectively. According to those values, *trans*-indigo will arrive to the detector first followed by *cis*-indigo. However, both protonated *cis*- and *trans*-isoindigo were given almost same CCS values (133.17 $Å^2$ and 133.44 $Å^2$). Protonated *cis* and *trans* indirubin gave two different CSS values, 134.62 $Å^2$ and 138.62 $Å^2$ respectively. So according to the predicted CCS values, protonated *cis*-indirubin will arrive to the detector faster than *trans*-indirubin.

Table 3.1 Predicted collision cross sections (CCS) for protonated indigo, protonated isoindigo and protonated indirubin

Isomer	Predicted CCS ($Å^2$)
Protonated cis-indigo	138.79
Protonated *trans*-indigo	136.50
Protonated *cis*-isoindigo	133.17
Protonated *trans*-isoindigo	133.44
Protonated *cis*-indirubin	134.62
Protonated *trans*-indirubin	138.62

Table 3.2 shows the calculated CCSs for sodiated indigoid isomers. The calculated CCS values are 238.55 $Å^2$, 214.36 $Å^2$ and 213.69 $Å^2$ for sodiated indigo, sodiated isoindigo and sodiated indirubin respectively. According to those values, sodiated indirubin will arrive to the detector first followed by sodiated isoindigo and sodiated indigo.

Table 3.2 Predicted collision cross sections (CCS) for sodiated indigo, sodiated isoindigo and sodiated indirubin

Isomer	Predicted CCS ($Å^2$)
Sodiated indigo	238.35
Sodiated isoindigo	214.36
Sodiated indirubin	213.69

Compared to the calculated CCS values of protonated isomers, sodiated isomers show significant difference. However, these results can be verified by following DTIMS experiments. The calculations were obtained using N_2 as the background gas. However, if the experiments are performed with a different background gas, the calculations need to be done with that corresponding gas before comparing with the experimental results.

3.3.2 Anthraquinone isomers

3.3.2.1 Comparison of theoretical IR spectra of sodiated and lithiated anthraquinone isomers

Previously, the IR spectra for different anthraquinone isomers were predicted for the protonated structure.[57] In the present study, the IR spectra of alizarin, anthrarufin, and chryzarin are predicted when bound with various cations. The lowest energy conformers of each sodiated isomers generated at B3LYP/6-31+G(d) level of theory are shown in Figure 3.11.

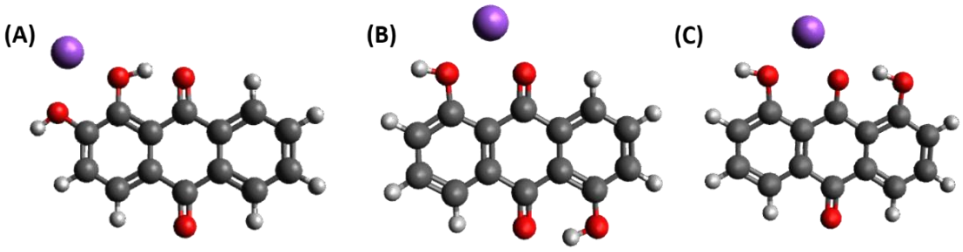

Figure 3.11 Lowest energy conformers of (A) sodiated alizarin, (B) sodiated anthrarufin and (C) sodiated chrysazin at B3LYP/6-31+G(d) level of theory

The predicted IR spectra of calculated lowest energy conformers for sodiated alizarin, sodiated anthrarufin, and sodiated chrysazin in both fingerprint and NH/OH stretching are shown in Figure 3.12. All the anthraquinone isomers have two C=O groups. Therefore C=O stretching can be used as a characteristic peak for differentiation of those isomers in fingerprint region. In sodiated alizarin, C=O stretching predicted at 1698 cm^{-1} and 1761 cm^{-1}, sodiated anthrarufin predicted at 1695 cm^{-1} and 1707 cm^{-1} whereas sodiated chrysazin predicted at 1688 cm^{-1} and 1760 cm^{-1}.

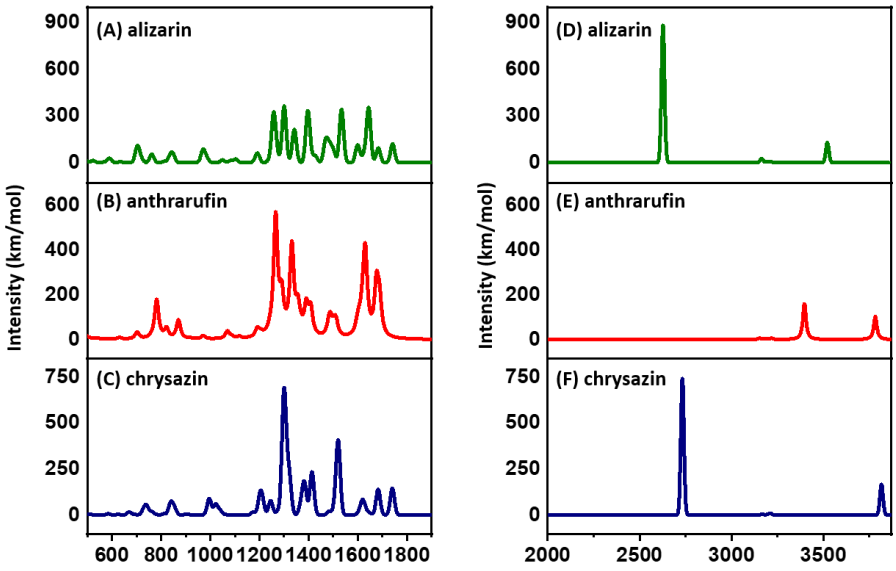

Figure 3.12 Comparison of theoretical infrared spectra of sodiated (A) alizarin, (B) anthrarufin, and (C) chrysazin in fingerprint region, sodiated (D) alizarin, (E) anthrarufin, and (F) chrysazin in NH/OH stretching region at B3LYP/6-31+G(d) level of theory

All three sodiated isomers showed distinct absorption bands in their IR spectra above 2500 cm^{-1} in NH/OH stretching region. Sodiated alizarin (Figure 3.12 (D)) shows two prominent absorption peaks at around 2500 cm^{-1} and 3840 cm^{-1} for the two different OH stretching modes. This difference is because of the two different environments of the OH groups. OH group closer to the carbonyl moiety shows the high intense absorption band. Theoretical spectrum of sodiated anthrarufin (Figure 3.12 (E)) also predicted two different absorption bands for OH stretching vibrations. The stretching mode of the free OH group is predicted at 3350 cm^{-1} whereas the OH group interacting with sodium cation shows absorption at 3807 cm^{-1}. Similarly, spectrum of sodiated chrysazin (Figure 3.12 (F)) also shows two different bands for OH stretching mode at

3806 cm^{-1} and 3450 cm^{-1}. Presence of this characteristic OH bands may be useful in distinguishing these sodiated isomers in the NH/OH stretching region theoretically.

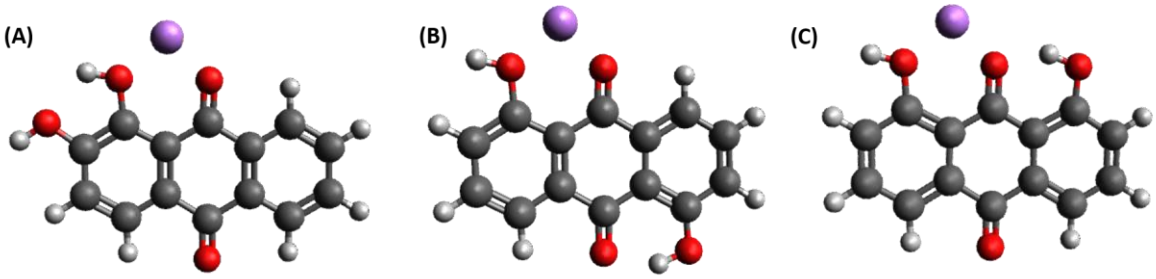

Figure 3.13 Lowest energy conformers of (A) lithiated alizarin, (B) lithiated anthrarufin and (C) lithiated chrysazin at B3LYP/6-311++G(d,p) level of theory

Figure 3.13 illustrates the structures of low energy conformers of lithiated isomers. Comparison of theoretical infrared spectra of lithiated anthraquinone isomers are shown in Figure 3.14 for both fingerprint and NH/OH stretching regions. Lithiated alizarin predicted two peaks for C=O stretching mode. One predicted at 1760 cm^{-1} and the other at 1684 cm^{-1}. Lithiated anthrarufin also predicted two peaks at 1681 cm^{-1} and 1708 cm^{-1} for C=O stretching mode. Lithiated chrysazin predicted C=O stretching mode at 1763 cm^{-1}.

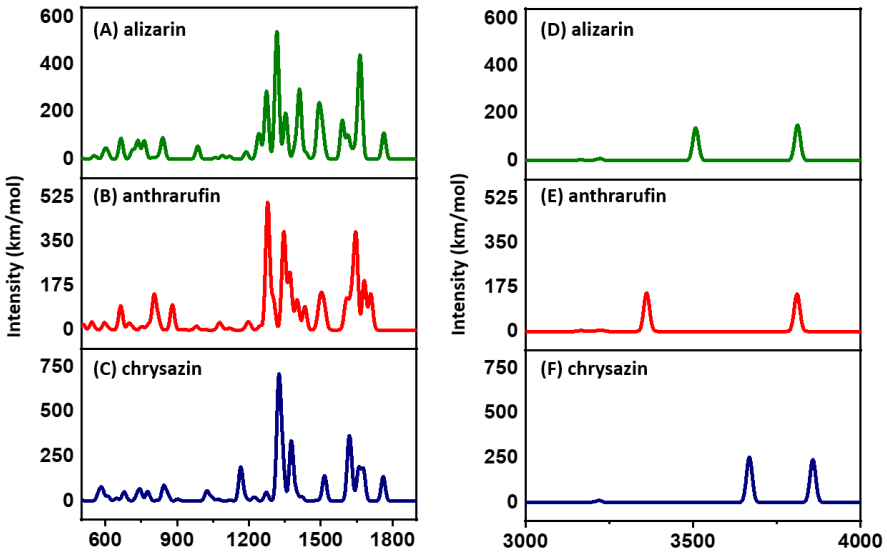

Figure 3.14 Comparison of theoretical infrared spectra of lithiated (A) alizarin, (B) anthrarufin, and (C) chrysazin in fingerprint region, lithiated (D) alizarin, (E) anthrarufin, and (F) chrysazin in NH/OH stretching region at B3LYP/6-31+G(d) level of theory

As observed in spectra of sodiated species, spectra of lithiated isomers also show two different absorption bands for the two different OH groups present in each isomer. Given the differences in the absorption bands, it can be predicted that sodiated and lithiated isomers can be distinguished based on the characteristic OH absorption band. However, the position of the absorption bands of OH mode predicted in spectra of lithiated isomers are different than that of sodiated isomers. According to the calculated spectra, lithiated alizarin shows bands at 3857 cm^{-1} and 3667 cm^{-1}, lithiated anthrarufin at 3810 cm^{-1} and 3361 cm^{-1} and lithiated chrysazin at 3811 cm^{-1} and 3507 cm^{-1} for OH stretching mode.

According to the calculations, theoretical spectra of sodiated and lithiated isomers show similar patterns in both fingerprint and OH/NH stretching regions. However, both spectra of

lithiated and sodiated isomers show characteristic bands in both regions. Therefore, IRMPD spectroscopy experiments can be carried out to differentiate these isomers (sodiated or lithiated) either in fingerprint or NH/OH stretching region for further investigation.

3.3.2.2 Comparison of theoretical collision cross sections of sodiated anthraquinone isomers

Table 3.3 shows the calculated collision cross sections for lowest energy conformers of sodiated isomers of anthraquinone at B3LYP/6-311++(d,p) level of theory. The predicted CCS values for sodiated alizarin, sodiated anthrarufin and sodiated chrysazin are 179.36 $Å^2$, 223.61 $Å^2$ and 224.45 $Å^2$ respectively. All the calculations were done at 298K. According to those values, sodiated alizarin will arrive to the detector first followed by sodiated anthrarufin and sodiated chrysazin while performing DTIMS experiments.

Experiment can be performed for the sodiated isomers to explore the separation in DTIMS study. Calculations were obtained with N_2 as the background gas. Therefore, if the experiments are carried with different background gas, the calculations need to be done with that corresponding gas before comparing with the experimental results.

Table 3.3 Predicted collision cross sections (CCS) for sodiated alizarin, sodiated anthrarufin and sodiated chrysazin

Isomer	Predicted CCS ($Å^2$)
Sodiated alizarin	179.36
Sodiated anthrarufin	223.61
Sodiated chrysazin	224.45

3.4 Conclusion

Theoretical IR spectra for the protonated indigoid isomers and sodiated indigoid isomers were obtained at B3LYP/6-31++G(d,p) level of theory. The predicted spectra of protonated and sodiated structural indigoid isomers showed characteristic bands in fingerprint region. The predicted spectra show distinct absorption patterns in *cis* and *trans* isomers of all three indigoid isomers in both fingerprint and NH/OH stretching regions. Protonated *cis* and *trans* forms of indigoid isomers show difference in each of their calculated CCS values. However, CCS values of sodiated isomers show significant difference compared to the protonated isomers.

Theoretical IR spectra of sodiated and lithiated anthraquinone isomers were predicted at B3LYP/6-31+G(d) method. Both IR spectra of sodiated and lithiated show different absorption patterns in both fingerprint and NH/OH stretching regions. Calculated CCS values show that sodiated alizarin will arrive to the detector first followed by sodiated anthrarufin and sodiated chrysazin while performing DTIMS experiments. However, IRMPD spectroscopy experiments and IMS studies can be carried out for further investigation.

CHAPTER IV

ONGOING WORK AND CONCLUSIONS

4.1 Ongoing work: Understanding the dissociation pathways of lithiated hydroxyproline isomers in the gas phase

In the process of analyzing the IRMPD spectroscopy data, it was found that the IRMPD-MS spectra exhibited interesting differences in dissociation patterns between lithiated *cis*3-hydroxyproline and lithiated *cis*-4-hyroxyproline. Specifically, water loss can be seen in lithiated *cis* hydroxyproline isomer but not in lithiated *cis*-4-hydroxyproline. To understand the physical chemistry reason behind these observations, I, along with a lab mate, are performing computational chemistry studies to model the thermodynamic and kinetic of the dissociation pathways. These investigations are ongoing.

4.2 Conclusions

Infrared multiple photon dissociation spectroscopy and ion mobility mass spectrometry are two main mass spectrometry strategies which can be used to differentiate the isomers. In this study theoretical approach was used to predict the experimental results. In the second chapter, experimental IRMPD spectra of *cis*-3, c*is*-4 and *trans*-4 hydroxyproline were interpreted with theoretical IR spectra obtained with density functional theory. Gas phase structural information were obtained with the computational studies. Theoretical spectra of lithiated positional isomers (*cis*-3 and c*is*-4) show more difference compared to the spectra of protonated positional isomers in both experiment and theoretical studies. According to the calculations, both lithiated *cis*-3 and

cis-4 hydroxyproline preferred to form charged solvated conformer whereas lithiated *trans*-hydroxyproline form salt bridge conformer as the lowest energy structure.

In chapter three, indigoid and anthraquinone dye isomers were studied with theoretical calculations. Theoretical IR spectra of protonated and sodiated indigoid showed characteristic bands (C=O stretching mode) in fingerprint region. Spectra of protonated stereoisomers (*cis* and *trans*) of indigoid dyes were presented in both fingerprint and OPO regions. Characteristic bands were obtained in both regions, C=O stretching band in fingerprint region and OH/NH bands in OPO region. Theoretical CCS values of sodiated indigoid isomers showed significant difference compared to CCS values of protonated isomers using N_2 as background gas. Similar patterns of theoretical spectra were obtained for both sodiated and lithiated anthraquinone isomers. Calculated CCS of sodiated isomers showed notable differences in the presence of N_2 as the background gas. IRMPD spectroscopy experiments and DTIMS studies can be carried out for further investigation of these indigoid and anthraquinone isomers.

REFERENCES

(1) Yerlekar, A.; Kshirsagar, M. A Review on Mass Spectrometry: Technique and Tools. *J. Eng. Res. Appl.* **2014**, *4* (4), 17–23.

(2) Gross, J. H. *Mass Spectrometry*, 2 nd.; Springer- Verlag Berlin Heidelberg, 2004.

(3) Kjeldsen, F.; Haselmann, K. F.; Sørensen, E. S.; Zubarev, R. A. Distinguishing of Ile/Leu Amino Acid Residues in the PP3 Protein by (Hot) Electron Capture Dissociation in Fourier Transform Ion Cyclotron Resonance Mass Spectrometry. *Anal. Chem.* **2003**, *75* (6), 1267–1274.

(4) Benjamin M. Davis, Glen F. Rall, M. J. S. Large-Scale Differentiation and Site Specific Discrimination of Hydroxyproline Isomers by Electron Transfer/Higher-Energy Collision Dissociation (EThcD) Mass Spectrometry. *Physiol. Behav.* **2017**, *176* (1), 139–148.

(5) Marinas, M.; Sa, E.; Rojas, M. M.; Moalem, M.; Urbano, F. J.; Guillou, C.; Rallo, L. Isomer Differentiation via Collision-Induced Dissociation: The Case of Protonated a-, B2- and B3-Phenylalanines and Their Derivatives. *Rapid Commun. Mass Spectrom.* **2010**, *24*, 1457–1466.

(6) Flick, T. G.; Campuzano, I. D. G.; Bartberger, M. D. Structural Resolution of 4-Substituted Proline Diastereomers with Ion Mobility Spectrometry via Alkali Metal Ion Cationization. *Anal. Chem.* **2015**.

(7) Crestoni, M. E.; Chiavarino, B.; Scuderi, D.; Di Marzio, A.; Fornarini, S. Discrimination of 4-Hydroxyproline Diastereomers by Vibrational Spectroscopy of the Gaseous Protonated Species. *J. Phys. Chem. B* **2012**, *116* (30), 8771–8779.

(8) Polfer, N. C. Infrared Multiple Photon Dissociation Spectroscopy of Trapped Ions. *Chem Soc Rev* **2011**, *40* (5), 2211–2221.

(9) Manz, C.; Grabarics, M.; Hoberg, F.; Pugini, M.; Stuckmann, A.; Struwe, W. B.; Pagel, K. Separation of Isomeric Glycans by Ion Mobility Spectrometry-the Impact of Fluorescent Labelling. *Analyst* **2019**, *144* (17), 5292–5298.

(10) Xie, C.; Wu, Q.; Zhang, S.; Wang, C.; Gao, W.; Yu, J.; Tang, K. Improving Glycan Isomeric Separation via Metal Ion Incorporation for Drift Tube Ion Mobility-Mass Spectrometry. *Talanta* **2020**, *211*, 120719.

(11) Patrick, A. L.; Stedwell, C. N.; Schindler, B.; Compagnon, I.; Berden, G.; Oomens, J.; Polfer, N. C. Insights into the Fragmentation Pathways of Gas-Phase Protonated Sulfoserine. *Int. J. Mass Spectrom.* **2015**, *379*, 209–214.

(12) Fenn, J. B.; Mann, M.; Meng, C. K.; Wong, S. F.; Whitehouse, C. M. Electrospray Ionization for Mass Spectrometry of Large Biomolecules. *Science (80-.).* **1989**, *246* (4926), 64–71.

(13) Wilm, M. Principles of Electrospray Ionization. *Mol. Cell. Proteomics* **2011**, *10* (7), 1–8.

(14) Kebarle, P.; Verkcerk, U. H. Electrospray: From Ions in Solution to Ions in the Gas Phase, What We Know Now. *Mass Spectrom. Rev.* **2009**, *28* (6), 898–917.

(15) Taylor, G. Disintegration of Pairs of Water Drops in an Electric Field. *Proc. R. Soc. London. Ser. A. Math. Phys. Sci.* **1966**, *295* (1440), 84–97.

(16) Cech, N. B.; Enke, C. G. Practical Implications of Some Recent Studies in Electrospray Ionization Fundamentals. *Mass Spectrom. Rev.* **2002**, *20* (6), 362–387.

(17) Rayleigh, Lord. On the Equilibrium of Liquid Conducting Masses Charged with Electricity. *Philos. Mag.* **1882**, *14* (87), 184–186.

(18) Konermann, L.; Ahadi, E.; Rodriguez, A. D.; Vahidi, S. Unraveling the Mechanism of Electrospray Ionization. *Anal. Chem.* **2013**, *85* (1), 2–9.

(19) Nguyen, S.; Fenn, J. B. Gas-Phase Ions of Solute Species from Charged Droplets of Solutions. *Proc. Natl. Acad. Sci. U. S. A.* **2007**, *104* (4), 1111–1117.

(20) Iribarne, J. V.; Thomson, B. A. On the Evaporation of Small Ions from Charged Droplets. *J. Chem. Phys.* **1976**, *64* (6), 2287–2294.

(21) Mack, L. L.; Kralik, P.; Rheude, A.; Dole, M. Molecular Beams of Macroions. II. *J. Chem. Phys.* **1970**, *52* (10), 4977–4986.

(22) Schmelzeisen-Redeker, G.; Bütfering, L.; Röllgen, F. W. Desolvation of Ions and Molecules in Thermospray Mass Spectrometry. *Int. J. Mass Spectrom. Ion Process.* **1989**, *90* (2), 139–150.

(23) Winger, B. E.; Light-wahl, K. J.; Loo, R. R. O.; Udseth, H. R.; Smith, R. D. Observation and Implications of High Mass-to-Charge Ratio Ions from Electrospray Ionization Mass Spectrometry. *J Am Soc Mass Spectrom.* **1993**, *4(7)*, 536–545.

(24) Kebarle, P. A Brief Overview of the Present Status of the Mechanisms Involved in Electrospray Mass Spectrometry. *J. Mass Spectrom.* **2000**, *35* (7), 804–817.

(25) Ein Neues Massenspektrometer Ohne Magnetfeld. *Paul W. Steinwedel H.* **1953**, *8* (7), 448–450.

(26) Martens, J.; Berden, G.; Gebhardt, C. R.; Oomens, J. Infrared Ion Spectroscopy in a Modified Quadrupole Ion Trap Mass Spectrometer at the FELIX Free Electron Laser Laboratory. *Rev. Sci. Instrum.* **2016**, *103108*.

(27) March, R. E. An Introduction to Quadrupole Ion Trap Mass Spectrometry. *J. Mass Spectrom.* **1997**, *32* (4), 351–369.

(28) Mathieu, É. Thesis on the Vibratory Movement of an Elliptical Membrane. *J. Pure Appl. Math.* **1868**, *13*, 137–203.

(29) March, R. E. Quadrupole Ion Traps. **2009**, 961–989.

(30) Brodbelt, J. S.; Wilson, J. J. Infrared Multiphoton Dissociation in Quadrupole Ion Traps. *Mass Spectrom. Rev.* **2009**, *28* (3), 390–424.

(31) Scoles, K. K. L. and G.; Department. Intramolrcular Dynamics From Eigenstate -Resolved Infrared Spectra. *Annu. Rev. Phys.* **1994**, *45*, 241.

(32) Woodin, R. L.; Bomse, D. S.; Beauchamp, J. L. Multiphoton Dissociation of Molecules with Low Power Continuous Wave Infrared Laser Radiation. *J. Am. Chem. Soc.* **1978**, *100* (10), 3248–3250.

(33) O'Shea, P. G.; Freund, H. P. Free-Electron Lasers: Status and Applications. *Science (80-.).* **2001**, *292* (5523), 1853–1858.

(34)) J. A. Giordmaine and Robert C. Miller. Tunable Coherent Parametric Oscillation in LiNb**O**$_3$ at Optical Frequencies. *Phys. Rev. Lett.* **1965**, *14* (24), 973–976.

(35) Polfer, N. C. Infrared Multiple Photon Dissociation Spectroscopy of Trapped Ions. *Chem. Soc. Rev.* **2011**, *40* (5), 2211–2221.

(36) Bakker, R. J.; Van Der Geer, C. A. J.; Jaroszynski, D. A.; Van Der Meer, A. F. G.; Oepts, D.; Van Amersfoort, P. W. Broadband Tunability of a Far-Infrared Free-Electron Laser. *J. Appl. Phys.* **1993**, *74* (3), 1501–1509.

(37) Adrien Marchand, Sandrine Livet, Frédéric Rosu, and V. G. Drift Tube Ion Mobility: How to Reconstruct Collision Cross Section Distributions from Arrival Time Distributions? *Anal Chem.* **2017**, *89(23)*, 12674-12681.

(38) Hill, H. H.; William, F.; Louis, R. H. S.; Mcminn, D. G. Spectrometry. **1974**, *1201* (1), 1201–1209.

(39) Creaser, C. S.; Griffiths, J. M. R.; Bramwell, C. J.; Noreen, S.; Hill, C. A.; Thomas, C. L. P. Ion Mobility Spectrometry: A Review. Part 1. Structural Analysis by Mobility Measurement. *Analyst* **2004**, *129* (11), 984–994.

(40) Revercomb, H. E.; Mason, E. A. Theory of Plasma Chromatography/Gaseous Electrophoresis. A Review. *Anal. Chem.* **1975**, *47* (7), 970–983.

(41) Reid Asbury, G.; Hill, H. H. Using Different Drift Gases to Change Separation Factors (a) in Ion Mobility Spectrometry. *Anal. Chem.* **2000**, *72* (3), 580–584.

(42) Xie, C.; Wu, Q.; Zhang, S.; Wang, C.; Gao, W.; Yu, J.; Tang, K. Improving Glycan Isomeric Separation via Metal Ion Incorporation for Drift Tube Ion Mobility-Mass Spectrometry. *Talanta* **2020**, *211*, 120719.

(43) Zietek, B. M.; Mengerink, Y.; Jordens, J.; Somsen, G. W.; Kool, J.; Honing, M. Adduct-Ion Formation in Trapped Ion Mobility Spectrometry as a Potential Tool for Studying Molecular Structures and Conformations. *Int. J. Ion Mobil. Spectrom.* **2018**, *21* (1–2), 19–32.

(44) Lee, J. W.; Lee, H. H. L.; Davidson, K. L.; Bush, M. F.; Kim, H. I. Structural Characterization of Small Molecular Ions by Ion Mobility Mass Spectrometry in Nitrogen Drift Gas: Improving the Accuracy of Trajectory Method Calculations. *Analyst* **2018**, *143* (8), 1786–1796.

(45) Verma, P.; Truhlar, D. G. Status and Challenges of Density Functional Theory. *Trends Chem.* **2020**, *2* (4), 302–318.

(46) Frank Jesen. *Introduction to Computational Chemsitry*. 2nd ed.,Wiley, 2007.

(47) Acharya, B.; Kaushalya, W. K. D. N.; Martens, J.; Berden, G.; Oomens, J.; Patrick, A. L. A Combined Infrared Ion Spectroscopy and Computational Chemistry Study of Hydroxyproline Isomers. *J. Am. Soc. mass Spectrom.* **2020**, *31* (6), 1205–1211.

(48) Dunbar, R. C.; Steill, J. D.; Oomens, J. Cationized Phenylalanine Conformations Characterized by IRMPD and Computation for Singly and Doubly Charged Ions. *Phys. Chem. Chem. Phys.* **2010**, *12* (41), 13383–13393.

(49) Wu, R.; McMahon, T. B. An Investigation of Protonation Sites and Conformations of Protonated Amino Acids by IRMPD Spectroscopy. *ChemPhysChem* **2008**, *9* (18), 2826–2835.

(50) Munshi, M. U.; Martens, J.; Berden, G.; Oomens, J. Protoisomerization of Indigo and Isoindigo Dyes Confirmed by Gas-Phase Infrared Ion Spectroscopy. *com* **2019**, *123* (38), 8226–8233.

(51) Nieckarz, R. J.; Oomens, J.; Berden, G.; Sagulenko, P.; Zenobi, R. Infrared Multiple Photon Dissociation (IRMPD) Spectroscopy of Oxazine Dyes. *Phys. Chem. Chem. Phys.* **2013**, *15* (14), 5049–5056.

(52) Becke, A. D. Density-Functional Thermochemistry. III. The Role of Exact Exchange. *J. Chem. Phys.* **1993**, *98* (7), 5648–5652.

(53) Dunbar, R. C.; Berden, G.; Oomens, J. How Does a Small Peptide Choose How to Bind a Metal Ion? IRMPD and Computational Survey of CS versus Iminol Binding Preferences. *Int. J. Mass Spectrom.* **2013**, *354–355*, 356–364.

(54) Zhao, Y.; Truhlar, D. G. The M06 Suite of Density Functionals for Main Group Thermochemistry, Thermochemical Kinetics, Noncovalent Interactions, Excited States, and Transition Elements: Two New Functionals and Systematic Testing of Four M06-Class Functionals and 12 Other Function. *Theor. Chem. Acc.* **2008**, *120* (1–3), 215–241.

(55) Levine, I. N. *Quantum Chemistry Pearson Advanced Chemistry Series*; 2014.

(56) Foresman, J. B.; Frisch, A. Exploring Chemistry with Electronic Structure Methods. 3rd Edition Ed. *Gaussian Inc.* **2015**.

(57) Pagliai, M.; Cardini, G.; Osticioli, I.; Nevin, A.; Schettino, V.; Siano, S.; Ugo, C. DFT Calculations of the IR and Raman Spectra of Anthraquinone Dyes and Lakes. **2018**, No. October 2017, 668–683.

(58) Scott, A. P.; Radom, L. Harmonic Vibrational Frequencies: An Evaluation of Hartree-Fock, Møller-Plesset, Quadratic Configuration Interaction, Density Functional Theory, and Semiempirical Scale Factors. *J. Phys. Chem.* **1996**, *100* (41), 16502–16513.

(59) Andersson, M. P.; Uvdal, P. New Scale Factors for Harmonic Vibrational Frequencies Using the B3LYP Density Functional Method with the Triple-ζ Basis Set 6-311+G(d,P). *J. Phys. Chem. A* **2005**, *109* (12), 2937–2941.

(60) V. D'Atri , M. Porrini, F. R. and V. G. Linking Molecular Models with Ion Mobility Experiments . Illustration with a Rigid Nucleic Acid Structure. *J. Mass Spectrom.* **2015**, *50*, 711–726.

(61) Zakharova, N. L.; Crawford, C. L.; Hauck, B. C.; Quinton, J. K.; Seims, W. F.; Jr, H. H. H.; Clark, A. E. An Assessment of Computational Methods for Obtaining Structural Information of Moderately Flexible Biomolecules from Ion Mobility Spectrometry. *J. Mass Spectrom.* **2012**, 792–805.

(62) Lee, J. W.; Davidson, K. L.; Bush, M. F.; Kim, H. I. Collision Cross Sections and Ion Structures: Development of a General Calculation Method via High-Quality Ion Mobility

Measurements and Theoretical Modeling. *Analyst* **2017**, *142* (22), 4289–4298.

(63) Gabelica, V.; Marklund, E. Fundamentals of Ion Mobility Spectrometry. *Curr. Opin. Chem. Biol.* **2018**, *42*, 51–59.

(64) Takaya, K.; Kaneko, T.; Tanuma, H.; Nishide, T.; Sugiyama, H.; Nakano, N.; Nagashima, H.; Seto, Y. Model Calculation for Ion Mobility in Air Using the MOBCAL Program. *Int. J. Ion Mobil. Spectrom.* **2016**, *19* (4), 227–232.

(65) Ewing, S. A.; Donor, M. T.; Wilson, J. W.; Prell, J. S. Sections with the Trajectory Method. **2018**, *28* (4), 587–596.

(66) Gorres, K. L.; Raines, R. T. Prolyl 4-Hydroxylase. *Crit. Rev. Biochem. Mol. Biol.* **2010**, *45* (2), 106–124.

(67) Shoulders, M. D.; Raines, R. T. Collagen Structure and Stability. *Annu. Rev. Biochem.* **2009**, *78* (1), 929–958.

(68) Mori, H.; Shibasaki, T.; Uozaki, Y.; Ochiai, K.; Ozaki, A. Detection of Novel Proline 3-Hydroxylase Activities in Streptomyces and Bacillus Spp. by Regio- and Stereospecific Hydroxylation of L-Proline. *Appl. Environ. Microbiol.* **1996**, *62* (6), 1903–1907.

(69) Gasser, A. B.; Depierre, D.; Courvoisier, B. Total Urinary and Free Serum Hydroxyproline in Metastatic Bone Disease. *Br. J. Cancer* **1979**, *39* (3), 280–283.

(70) Eric F. Strittmatter, Andrew S. Lemoff, and E. R. W. Structure of Cationized Glycine, Gly·M2+ (M = Be, Mg, Ca, Sr, Ba), in the Gas Phase: Intrinsic Effect of Cation Size on Zwitterion Stability. *J. Phys. Chem. A* **2006**, *104* (43), 9793–9796.

(71) Cerda, B. A.; Wesdemiotis, C. Zwitterionic vs. Charge-Solvated Structures in the Binding of Arginine to Alkali Metal Ions in the Gas Phase. *Analyst* **2000**, *125* (4), 657–660.

(72) Jensen, F. Structure and Stability of Complexes of Glycine and Glycine Methyl Analogs with H+, Li+, and Na+. *J. Am. Chem. Soc.* **1992**, *114* (24), 9533–9537.

(73) Ryzhov, V.; Dunbar, R. C. Cation ?Effects in the Complexation of Naɦ and Kɦ with Phe, Tyr, and Trp in Thethe Gas Phase. **2000**, *0305* (00), 7777–7783.

(74) Wyttenbach, T.; Witt, M.; Bowers, M. T.; Barbara, S.; July, R. V; Re, V.; Recei, M.; February, V. On the Stability of Amino Acid Zwitterions in the Gas Phase : The Influence of Derivatization , Proton Affinity , and Alkali Ion Addition. **2000**, No. 8, 3458–3464.

(75) Moision, R. M.; Armentrout, P. B. Experimental and Theoretical Dissection of Sodium Cation/Glycine Interactions. *J. Phys. Chem. A* **2002**, *106* (43), 10350–10362.

(76) Jockusch, R. A.; Price, W. D.; Williams, E. R. Structure of Cationized Arginine (Arg·M+, H = H, Li, Na, K, Rb, and Cs) in the Gas Phase: Further Evidence for Zwitterionic Arginine. *J. Phys. Chem. A* **1999**, *103* (46), 9266–9274.

(77) Polfer, N. C.; Dunbar, R. C. IRMPD Spectroscopy of Metal-Ion/Tryptophan Complexes. *Phys. Chem. Chem. Phys.* **2006**, 2744–2751.

(78) Kapota, C.; Maı, P.; Ohanessian, G. Vibrational Signature of Charge Solvation vs Salt Bridge Isomers of Sodiated Amino Acids in the Gas Phase. **2004**, No. 3, 1836–1842.

(79) Forbes, M. W.; Bush, M. F.; Polfer, N. C.; Oomens, J.; Dunbar, R. C.; Williams, E. R.; Jockusch, R. A. Infrared Spectroscopy of Arginine Cation Complexes : Direct Observation of Gas-Phase Zwitterions. *J. Phys. Chem. A* **2007**, 11759–11770.

(80) Drayß, M. K.; Armentrout, P. B.; Oomens, J.; Schäfer, M. IR Spectroscopy of Cationized Aliphatic Amino Acids: Stability of Charge-Solvated Structure Increases with Metal Cation Size. *Int. J. Mass Spectrom.* **2010**, *297* (1–3), 18–27.

(81) Armentrout, P. B.; Armentrout, E. I.; Clark, A. A.; Cooper, T. E.; Stennett, E. M. S.; Carl, D. R. An Experimental and Theoretical Study of Alkali Metal Cation Interactions with Cysteine. *J. Phys. Chem. B* **2010**, *114* (11), 3927–3937.

(82) Frisch, M. J.; Trucks, G. W.; Schlegel, H. B.; Scuseria, G. E.; Robb, M. A.; Cheeseman, J. R.; Scalmani, G.; Barone, V.; Mennucci, B.; Petersson, G. A.; Nakatsuji, H.; Caricato, M.; Li, X.; Hratchian, H. P.; Izmaylov, A. F.; Bloino, J.; Zheng, G.; Sonnenberg, J. L.; Hada, M.; Ehara, M.; Toyota, K.; Fukuda, R.; Hasegawa, J.; Ishida, M.; Nakajima, T.; Honda, Y.; Kitao, O.; Nakai, H.; Vreven, T.; Montgomery, J. A., Jr.; Peralta, J. E.; Ogliaro, F.; Bearpark, M.; Heyd, J. J.; Brothers, E.; Kudin, K. N.; Staroverov, V. N.; Kobayashi, R.; Normand, J.; Raghavachari, K.; Rendell, A.; Burant, J. C.; Iyengar, S. S.; Tomasi, J.; Cossi, M.; Rega, N.; Millam, J. M.; Klene, M.; Knox, J. E.; Cross, J. B.; Bakken, V.; Adamo, C.; Jaramillo, J.; Gomperts, R.; Stratmann, R. E.; Yazyev, O.; Austin, A. J.; Cammi, R.; Pomelli, C.; Ochterski, J. W.; Martin, R. L.; Morokuma, K.; Zakrzewski, V. G.; Voth, G. A.; Salvador, P.; Dannenberg, J. J.; Dapprich, S.; Daniels, A. D.; Farkas, O.; Foresman, J. B.; Ortiz, J. V.; Cioslowski, J.; Fox, D. J. *Gaussian 09*, Revision D.01; Gaussian, Inc.: Wallingford, CT, 2016.

(83) Oomens, J.; Steill, J. D. The Structure of Deprotonated Tri-Alanine and Its a 3- Fragment Anion by IR Spectroscopy. *J. Am. Soc. Mass Spectrom.* **2010**, *21* (5), 698–706.

(84) Munshi, M. U.; Berden, G.; Martens, J.; Oomens, J. Gas-Phase Vibrational Spectroscopy of Triphenylamine: The Effect of Charge on Structure and Spectra. *Phys. Chem. Chem. Phys.* **2017**, *19* (30), 19881–19889.

(85) Li, H. *Conformations of Amino Acids Characterized by Theoretical*; Ph.D. Thesis. 2014.

(86) Hanwell, M. D.; Curtis, D. E.; Lonie, D. C.; Vandermeersch, T.; Zurek, E.; Hutchison, G.

R. Avogadro : An Advanced Semantic Chemical Editor , Visualization , and Analysis Platform. **2012**, 1–17.

(87) Allouche, A.-R. Gabedit—A Graphical User Interface for Computational Chemistry Softwares. *J. Comput. Chem.* **2011**, *32* (1), 174–182.

(88) Kapota, C.; Maı, P.; Ohanessian, G. Vibrational Signature of Charge Solvation vs Salt Bridge Isomers of Sodiated Amino Acids in the Gas Phase. **2004**, No. 3, 1836–1842.

(89) Degano, I.; Ribechini, E.; Modugno, F.; Colombini, M. P. Analytical Methods for the Characterization of Organic Dyes in Artworks and in Historical Textiles. *Appl. Spectrosc. Rev.* **2009**, *44* (5), 363–410.

(90) Cardon, D. *Natural Dyes*; Archetype Books, London, 2000.

(91) Bechtold, T.; Mussak, R. *Handbook of Natural Colorants*, 2009.

(92) Ballard, M. W. Natural Dyes: Sources, Tradition, Technology and Science. *Stud. Conserv.* **2007**, *52* (4), 318–319.

(93) Jorgensen, L. B.; Walton, P. Dyes and Fleece Types in Prehistoric Textiles from Scandinavia and Germany. *J. Danish Archaeol.* **1986**, *5* (1), 177–188.

(94) Bender, M. Colors for Textiles in Ancient and Modern. *J. Chem. Educ.* **1947**, *24* (1), 2–10.

(95) Ferreira, E. S. B.; Hulme, A. N.; McNab, H.; Quye, A. The Natural Constituents of Historical Textile Dyes. *Chem. Soc. Rev.* **2004**, *33* (6), 329–336.

(96) Głowacki, E. D.; Voss, G.; Sariciftci, N. S. 25th Anniversary Article: Progress in Chemistry and Applications of Functional Indigos for Organic Electronics. *Adv. Mater.* **2013**, *25* (47), 6783–6800.

(97) Eisenbrand, G.; Hippe, F.; Jakobs, S.; Muehlbeyer, S. Molecular Mechanisms of Indirubin and Its Derivatives: Novel Anticancer Molecules with Their Origin in Traditional Chinese Phytomedicine. *J. Cancer Res. Clin. Oncol.* **2004**, *130* (11), 627–635.

(98) Sassatelli, M.; Saab, E.; Anizon, F.; Prudhomme, M.; Moreau, P. Synthesis of Glycosyl-Isoindigo Derivatives. *Tetrahedron Lett.* **2004**, *45* (25), 4827–4830.

(99) Voronina, Y. K.; Krivolapov, D. B.; Bogdanov, A. V.; Mironov, V. F.; Litvinov, I. A. An Unusual Conformation of 1,1'-Dimethylisoindigo in Crystals. *J. Struct. Chem.* **2012**, *53* (2), 413–416.

(100) Crossley, M. L. Certain Metallic Derivatives of Hydroxy-Anthraquinones. *J. Am. Chem.*

Soc. **1919**, *41* (12), 2081–2083.

(101) Eberle, A. R.; Lerner, M. W. Separation and Determination of Scandium Spectrophotometric Method Using Alizarin Red S. *Anal. Chem.* **1955**, *27* (10), 1551–1554.

(102) Natelson, S.; Penniall1, R. Colorimetric Estimation of Ultramicro Quantities of Calcium in Human Serum as the Complex with Alizarin. *Anal. Chem.* **1955**, *27* (3), 434–437.

(103) Gregory, C. A.; Gunn, W. G.; Peister, A.; Prockop, D. J. An Alizarin Red-Based Assay of Mineralization by Adherent Cells in Culture: Comparison with Cetylpyridinium Chloride Extraction. *Anal. Biochem.* **2004**, *329* (1), 77–84.

(104) Ladell, P. Isolation and Characterization of Antibiotics produced by the Nematode Symbiont Xenorhabdus Szentiramaii.Master Thesis. **2011**.

(105) Say-Liang-Fat, S.; Cornard, J. P.; Moncomble, A. Study on Chrysazin-Aluminium(III) Interaction in Solution by Spectroscopy and Quantum Chemical Calculations. *Polyhedron* **2012**, *48* (1), 237–244.

(106) Kramell, A. E.; Brachmann, A. O.; Kluge, R.; Piel, J.; Csuk, R. Fast Direct Detection of Natural Dyes in Historic and Prehistoric Textiles by Flowprobe^{TM}-ESI-HRMS. *RSC Adv.* **2017**, *7* (21), 12990–12997.

(107) Orska-Gawryś, J.; Surowiec, I.; Kehl, J.; Rejniak, H.; Urbaniak-Walczak, K.; Trojanowicz, M. Identification of Natural Dyes in Archeological Coptic Textiles by Liquid Chromatography with Diode Array Detection. *J. Chromatogr. A* **2003**, *989* (2), 239–248.

(108) Surowiec, I.; Quye, A.; Trojanowicz, M. Liquid Chromatography Determination of Natural Dyes in Extracts from Historical Scottish Textiles Excavated from Peat Bogs. *J. Chromatogr. A* **2006**, *1112* (1–2), 209–217.

(109) Puchalska, M.; Połeć-Pawlak, K.; Zadrozna, I.; Hryszko, H.; Jarosz, M. Identification of Indigoid Dyes in Natural Organic Pigments Used in Historical Art Objects by High-Performance Liquid Chromatography Coupled to Electrospray Ionization Spectrometry. *J. Mass Spectrom.* **2004**, *39* (12), 1441–1449.

(110) Surowiec, I.; Szostek, B.; Trojanowicz, M. HPLC-MS of Anthraquinoids, Flavonoids, and Their Degradation Products in Analysis of Natural Dyes in Archeological Objects. *J. Sep. Sci.* **2007**, *30* (13), 2070–2079.

(111) Pauk, V.; Barták, P.; Lemr, K. Characterization of Natural Organic Colorants in Historical and Art Objects by High-Performance Liquid Chromatography. *J. Sep. Sci.* **2014**, *37* (23), 3393–3410.

(112) Degani, L.; Riedo, C.; Gulmini, M.; Chiantore, O. From Plant Extracts to Historical Textiles: Characterization of Dyestuffs by GC–MS. *Chromatographia* **2014**, *77* (23–24), 1683–1696.

(113) Degani, L.; Riedo, C.; Chiantore, O. Identification of Natural Indigo in Historical Textiles by GC–MS. *Anal. Bioanal. Chem.* **2015**, *407* (6), 1695–1704.

(114) Zou, P.; Koh, H. L. Determination of Indican, Isatin, Indirubin and Indigotin in Isatis Indigotica by Liquid Chromatography/Electrospray Ionization Tandem Mass Spectrometry. *Rapid Commun. Mass Spectrom.* **2007**, *21* (7), 1239–1246.

(115) Lech, K.; Jarosz, M. Identification of Polish Cochineal (Porphyrophora Polonica L.) in Historical Textiles by High-Performance Liquid Chromatography Coupled with Spectrophotometric and Tandem Mass Spectrometric Detection. *Anal. Bioanal. Chem.* **2016**, *408* (12), 3349–3358.

(116) Hajjar, L.; Hicks, R. G.; Zeng, T. A Computational Study of the Protoisomerization of Indigo and Its Imine Derivatives. *J. Phys. Chem. A* **2016**, *120* (38), 7569–7576.

(117) Chatterjee, P.; Dutta, S.S.; Chakraborty, T. Isomers and Rotamers of DCM in Methanol and in Gas Phase Probed by Ion Mobility Mass Spectrometry in Combination with High Performance Liquid Chromatography. *J. Phys. Chem. B* **2020**, *124*(22), 4498–4511.

(118) Allouche, A. Software News and Updates Gabedit — A Graphical User Interface for Computational Chemistry Softwares. *J. Comput. Chem.* **2012**, *32*, 174–182.

(119) Scott, A. P.; Radom, L. Harmonic Vibrational Frequencies: An Evaluation of Hartree−Fock, Møller−Plesset, Quadratic Configuration Interaction, Density Functional Theory, and Semiempirical Scale Factors. **1996**, *3654* (d), 16502–16513.

(120) Laury, M. L.; Carlson, M. J.; Wilson, A. K. Vibrational Frequency Scale Factors for Density Functional Theory and the Polarization Consistent Basis Sets. **2012**.

(121) Munshi, M. U.; Craig, S. M.; Berden, G.; Martens, J.; Deblase, A. F.; Foreman, D. J.; McLuckey, S. A.; Oomens, J.; Johnson, M. A. Preparation of Labile Ni+(Cyclam) Cations in the Gas Phase Using Electron-Transfer Reduction through Ion-Ion Recombination in an Ion Trap and Structural Characterization with Vibrational Spectroscopy. *J. Phys. Chem. Lett.* **2017**, *8* (20), 5047–5052.

(122) Fricke, H.; Gerlach, A.; Gerhards, M. Structure of a β-Sheet Model System in the Gas Phase: Analysis of the Fingerprint Region up to 10 Mm. *Phys. Chem. Chem. Phys.* **2006**, *8* (14), 1660–1662.

(123) Filippi, A.; Fraschetti, C.; Rondino, F.; Piccirillo, S.; Steinmetz, V.; Guidoni, L.;

Speranza, M. International Journal of Mass Spectrometry Protonated Pyrimidine Nucleosides Probed by IRMPD Spectroscopy. *Int. J. Mass Spectrom.* **2013**, *354–355*, 54–61.

(124) Emma C. Nicholls-Allison, a Graeme Nawna, B. O. P. and R. G. H. Protoisomerization of Indigo Di- and Monoimines Emma. *J. Mater. Chem. B* **2018**, *6* (35).

(125) Rekik, N.; Ghalla, H.; Hanna, G. Explaining the Structure of the Oh Stretching Band in the Ir Spectra of Strongly Hydrogen-Bonded Dimers of Phosphinic Acid and Their Deuterated Analogs in the Gas Phase: A Computational Study. *J. Phys. Chem. A* **2012**, *116* (18), 4495–4509.

APPENDIX A

COORDINATES OF THE LOWEST ENERGY CONFORMERS OF INDIGOID ISOMERS

Coordinates of the optimized structures of lowest energy conformer of protonated cis indigo at B3LYP level with the basis set 6-31++G(d, p)

1	1		
C	-3.985302	-1.734666	-0.060200
C	-5.212054	-1.069149	-0.035115
C	-5.310539	0.340627	0.031673
C	-4.170256	1.124238	0.066791
C	-2.919494	0.470393	0.033358
C	-1.590391	0.966836	0.022286
C	-0.692464	-0.189646	-0.020591
N	-1.500334	-1.326610	-0.006860
C	-2.838766	-0.944803	-0.019136
H	-4.222446	2.206623	0.113931
H	-6.290614	0.803899	0.053940
H	-6.124327	-1.657003	-0.063959
H	-3.936185	-2.817612	-0.102755
C	3.982379	-1.722847	0.063275
C	5.225691	-1.071130	0.043727
C	5.335801	0.328195	-0.014404
C	4.192695	1.125167	-0.051670
C	2.946112	0.486606	-0.031301
C	1.598682	1.015665	-0.041969
C	0.685505	-0.195598	-0.003438
N	1.494897	-1.293215	0.023110
C	2.855522	-0.917137	0.023442
H	4.254386	2.207622	-0.093375
H	6.318037	0.787271	-0.029168
H	6.129162	-1.672076	0.073342
H	3.920073	-2.805310	0.105634
O	-1.268853	2.219993	0.056458
O	1.222891	2.196441	-0.066105
H	-1.198164	-2.233779	-0.331326
H	-0.249908	2.351379	0.005423
H	1.187034	-2.240229	0.191361

Coordinates of the optimized structures of lowest energy conformer of protonated trans indigo at B3LYP level with the basis set 6-31++G(d, p)

1	1		
C	3.922718	1.606947	-0.000244
C	5.160376	0.984719	0.000200
C	5.303259	-0.432744	0.000564
C	4.198131	-1.253678	0.000533
C	2.912653	-0.649770	0.000105
C	1.599582	-1.149588	-0.000089
C	0.696148	-0.044669	-0.000488
N	1.464483	1.117703	-0.000782
C	2.787739	0.781728	-0.000299
H	4.314104	-2.333637	0.000688
H	6.298947	-0.862185	0.000836
H	6.056260	1.597619	0.000283
H	3.833936	2.687999	-0.000525
C	-4.003043	-1.507209	-0.000178
C	-5.241748	-0.840731	0.000156
C	-5.330406	0.557285	0.000464
C	-4.172136	1.342279	0.000436
C	-2.938180	0.691015	0.000131
C	-1.566099	1.202572	-0.000025
C	-0.686446	-0.055284	-0.000463
N	-1.507647	-1.117404	-0.000551
C	-2.869893	-0.713219	-0.000140
H	-4.221758	2.426301	0.000651
H	-6.305236	1.032415	0.000731
H	-6.152303	-1.431369	0.000167
H	-3.951623	-2.591098	-0.000452
O	1.130589	-2.406713	0.000039
O	-1.120014	2.338120	0.000284
H	1.055252	2.044886	-0.000133
H	1.843948	-3.062684	0.000704
H	-1.189904	-2.079498	-0.000185

Coordinates of the optimized structures of lowest energy conformer of protonated cis isoindigo at B3LYP level with the basis set 6-31++G(d, p)

1	1		
C	2.592520	-1.416823	-0.445586
C	3.986450	-1.480484	-0.562352
C	4.790963	-0.357410	-0.348154
C	4.221234	0.881582	-0.017231
C	2.844225	0.919455	0.099307
N	2.028622	2.037799	0.395695
C	0.748263	1.698751	0.363156
C	0.612083	0.275829	0.037685
C	1.999980	-0.195056	-0.096914
O	-0.141113	2.592012	0.737701
C	-2.484757	1.335058	-0.671160
C	-3.863940	1.498201	-0.736886
C	-4.724132	0.462276	-0.327219
C	-4.228976	-0.769024	0.110572
C	-2.849159	-0.926862	0.171380
N	-2.124085	-2.065886	0.489989
C	-0.765850	-1.871490	0.305569
C	-0.607401	-0.377501	-0.007227
C	-1.950940	0.129507	-0.158728
O	0.094638	-2.716846	0.432528
H	-4.901159	-1.577666	0.377408
H	-5.798023	0.609115	-0.383800
H	-4.280300	2.417522	-1.133601
H	-1.843086	2.106190	-1.088116
H	-2.510781	-2.982641	0.672021
H	2.355021	2.955225	0.678663
H	-1.047976	2.233869	0.742660
H	1.989711	-2.300384	-0.597124
H	4.835465	1.763245	0.134175
H	5.868762	-0.437786	-0.442093
H	4.449033	-2.427472	-0.819083

Coordinates of the optimized structures of lowest energy conformer of protonated trans isoindigo at B3LYP level with the basis set 6-31++G(d, p)

1	1		
C	2.592520	-1.416823	-0.445586
C	3.986450	-1.480484	-0.562352
C	4.790963	-0.357410	-0.348154
C	4.221234	0.881582	-0.017231
C	2.844225	0.919455	0.099307
N	2.028622	2.037799	0.395695
C	0.748263	1.698751	0.363156
C	0.612083	0.275829	0.037685
C	1.999980	-0.195056	-0.096914
O	-0.141113	2.592012	0.737701
C	-2.484757	1.335058	-0.671160
C	-3.863940	1.498201	-0.736886
C	-4.724132	0.462276	-0.327219
C	-4.228976	-0.769024	0.110572
C	-2.849159	-0.926862	0.171380
N	-2.124085	-2.065886	0.489989
C	-0.765850	-1.871490	0.305569
C	-0.607401	-0.377501	-0.007227
C	-1.950940	0.129507	-0.158728
O	0.094638	-2.716846	0.432528
H	-4.901159	-1.577666	0.377408
H	-5.798023	0.609115	-0.383800
H	-4.280300	2.417522	-1.133601
H	-1.843086	2.106190	-1.088116
H	-2.510781	-2.982641	0.672021
H	2.355021	2.955225	0.678663
H	-1.047976	2.233869	0.742660
H	1.989711	-2.300384	-0.597124
H	4.835465	1.763245	0.134175
H	5.868762	-0.437786	-0.442093
H	4.449033	-2.427472	-0.819083

Coordinates of the optimized structures of lowest energy conformer of protonated cis indirubin at B3LYP level with the basis set 6-31++G(d, p)

1	1		
C	-4.124170	0.736643	0.000142
C	-5.077435	-0.280411	0.000258
C	-4.678994	-1.627452	0.000195
C	-3.326848	-2.008435	0.000002
C	-2.392179	-0.986535	-0.000092
N	-0.983852	-1.069974	-0.000311
C	-0.407770	0.159936	-0.000266
C	-1.564554	1.160479	-0.000130
C	-2.772214	0.368546	-0.000029
O	-1.446935	2.394690	-0.000082
H	-3.042007	-3.055347	-0.000080
H	-5.438173	-2.403319	0.000280
H	-6.133506	-0.034675	0.000406
H	-4.408658	1.783692	0.000179
C	2.244787	-1.869621	-0.000139
C	3.531987	-2.414748	-0.000031
C	4.664130	-1.591617	0.000156
C	4.541584	-0.195630	0.000229
C	3.258283	0.322981	0.000129
N	2.857797	1.675597	0.000099
C	1.524432	1.779475	-0.000024
C	0.946197	0.432546	-0.000103
C	2.093616	-0.476601	-0.000038
O	0.959380	2.938336	-0.000056
H	5.417132	0.445289	0.000344
H	5.652853	-2.037908	0.000243
H	3.653378	-3.492542	-0.000103
H	1.398795	-2.548100	-0.000327
H	3.471435	2.481451	0.000398
H	-0.075742	2.842709	-0.000124
H	-0.477804	-1.942159	-0.000181

Coordinates of the optimized structures of lowest energy conformer of protonated trans indirubin at B3LYP level with the basis set 6-31++G(d, p)

1	1		
C	3.720815	-1.633059	0.000088
C	4.980311	-1.022144	-0.000077
C	5.094002	0.374041	-0.000229
C	3.963385	1.210486	-0.000232
C	2.729772	0.583318	-0.000107
N	1.438325	1.172256	-0.000006
C	0.451585	0.257090	-0.000001
C	1.162505	-1.125121	0.000066
C	2.595686	-0.809586	0.000041
O	0.605029	-2.202714	0.000286
H	4.066787	2.290778	-0.000310
H	6.080019	0.827602	-0.000351
H	5.876828	-1.632419	-0.000087
H	3.613020	-2.712853	0.000214
C	-2.348445	-1.717369	0.000067
C	-3.669054	-2.176072	-0.000009
C	-4.757768	-1.294418	-0.000168
C	-4.553583	0.088202	-0.000268
C	-3.236444	0.523392	-0.000196
N	-2.767344	1.857991	-0.000004
C	-1.432266	1.862200	0.000262
C	-0.919179	0.527651	0.000209
C	-2.114635	-0.334709	-0.000043
O	-0.672565	2.959779	0.000339
H	-5.387174	0.783391	-0.000441
H	-5.770175	-1.683999	-0.000229
H	-3.851100	-3.245682	0.000076
H	-1.523574	-2.414369	0.000122
H	-3.365889	2.674755	-0.000418
H	-1.175548	3.789317	-0.000021
H	1.280094	2.171816	0.000098

Coordinates of the optimized structures of lowest energy conformer of sodiated indigo at B3LYP level with the basis set 6-31++G(d, p)

1	1		
C	4.044879	1.480513	-0.000342
C	5.322077	0.900675	-0.000032
C	5.506141	-0.490506	0.000326
C	4.403309	-1.347482	0.000363
C	3.126351	-0.782722	0.000112
C	1.791812	-1.389745	0.000059
C	0.836072	-0.212346	-0.000271
N	1.583306	0.924795	-0.000540
C	2.957992	0.616472	-0.000228
H	4.523281	-2.426145	0.000623
H	6.511051	-0.898423	0.000559
H	6.191532	1.550819	-0.000078
H	3.922751	2.559043	-0.000645
C	-3.647024	-2.163996	0.000047
C	-4.932438	-1.635338	0.000057
C	-5.173546	-0.239703	-0.000015
C	-4.112506	0.649741	-0.000056
C	-2.797177	0.145467	-0.000021
C	-1.504949	0.782047	-0.000177
C	-0.530278	-0.311224	-0.000244
N	-1.225154	-1.514536	-0.000181
C	-2.575741	-1.261264	-0.000012
H	-4.299496	1.721044	-0.000043
H	-6.195094	0.124569	-0.000046
H	-5.779698	-2.314146	0.000108
H	-3.480969	-3.236209	0.000102
O	1.436260	-2.562899	0.000282
O	-1.201693	2.020269	-0.000223
H	-0.758046	-2.413250	0.000175
H	1.174048	1.848149	-0.000323
Na	-2.043892	3.955476	0.000614

Coordinates of the optimized structures of lowest energy conformer of sodiated isoindigo at B3LYP level with the basis set 6-31++G(d, p)

1	1		
C	-2.871870	1.441481	-0.241509
C	-4.265723	1.421521	-0.353273
C	-4.976997	0.218958	-0.311822
C	-4.311324	-1.009215	-0.166343
C	-2.934928	-0.971011	-0.051765
N	-2.050147	-2.060052	0.080113
C	-0.762491	-1.651366	0.132893
C	-0.768249	-0.141018	-0.023164
C	-2.182671	0.228561	-0.077663
O	0.197677	-2.404351	0.382035
H	-4.859289	-1.945818	-0.149719
H	-6.058887	0.227862	-0.397492
H	-4.800756	2.358006	-0.468832
H	-2.332698	2.377441	-0.257317
C	2.377958	-0.881362	-0.923505
C	3.769332	-0.924748	-1.072085
C	4.568859	0.133994	-0.603913
C	3.992322	1.268281	-0.028686
C	2.604694	1.301672	0.107944
N	1.808030	2.345985	0.546922
C	0.454007	2.063104	0.392331
C	0.386641	0.603923	-0.028563
C	1.777779	0.207895	-0.263531
O	-0.443276	2.848598	0.631200
H	4.605335	2.109860	0.277429
H	5.645943	0.090616	-0.730439
H	4.229835	-1.750324	-1.606691
H	1.761593	-1.664196	-1.353590
H	2.127515	3.274952	0.786543
H	-2.320220	-3.022980	0.230412
Na	2.228838	-2.497722	1.113681

Coordinates of the optimized structures of lowest energy conformer of sodiated indirubin at B3LYP level with the basis set 6-31++G(d, p)

1	1		
C	3.710617	-1.548528	-0.047533
C	4.989409	-1.003239	-0.062718
C	5.163881	0.394639	-0.100335
C	4.083105	1.283593	-0.126972
C	2.807559	0.729488	-0.115936
N	1.569520	1.370450	-0.139549
C	0.547992	0.459141	-0.147251
C	1.191188	-0.911108	-0.051585
C	2.614445	-0.671600	-0.077112
O	0.574884	-1.981241	0.116076
H	4.240026	2.356615	-0.154904
H	6.171485	0.799024	-0.109204
H	5.859331	-1.650447	-0.045751
H	3.553761	-2.622071	-0.021081
C	-2.326477	-1.264511	-0.720773
C	-3.662884	-1.684706	-0.751390
C	-4.689108	-0.824403	-0.329894
C	-4.409269	0.483633	0.079105
C	-3.080037	0.896315	0.098191
N	-2.565718	2.159579	0.379043
C	-1.193859	2.197057	0.187570
C	-0.783744	0.789720	-0.120603
C	-2.011559	0.018862	-0.237502
O	-0.472578	3.182967	0.294387
H	-5.211121	1.162759	0.350703
H	-5.719928	-1.162043	-0.360736
H	-3.913831	-2.660919	-1.155660
H	-1.545694	-1.883816	-1.154898
H	1.388564	2.369870	-0.100979
H	-3.109003	2.992156	0.563062
Na	-1.206019	-2.735570	1.125248

APPENDIX B

COORDINATES OF THE LOWEST ENERGY CONFORMERS OF ANTHRAQUINONE ISOMERS

Coordinates of the optimized structures of lowest energy conformer of sodiated alizarin at B3LYP level with the basis set 6-311++G(d, p)

1	1		
C	1.85276100	-0.22202900	-0.00006500
C	2.75134900	0.84899000	0.00046700
C	2.28874200	2.15447100	-0.00000600
C	0.92017400	2.41254200	-0.00020200
C	0.01273500	1.36297300	-0.00008500
C	0.47537500	0.03652700	-0.00002700
C	-0.45018200	-1.10324100	0.00002100
C	-1.88962900	-0.84146400	0.00006500
C	-2.37372000	0.48160600	-0.00002600
C	-1.45147900	1.64953200	-0.00010500
C	-3.74738800	0.70836400	-0.00001300
C	-4.63129400	-0.36503400	0.00007900
C	-4.15157500	-1.67462500	0.00018000
C	-2.78490300	-1.91487200	0.00018500
H	-2.39405300	-2.92576100	0.00025200
H	-4.84649200	-2.50705100	0.00026800
H	-5.70029000	-0.18141700	0.00008900
H	-4.10415900	1.73206100	-0.00008200
O	0.00712600	-2.26120200	0.00007800
H	0.54575500	3.42941500	-0.00041400
H	2.99620900	2.97953000	0.00009600
O	4.09273700	0.51782600	0.00057000
O	2.32872200	-1.48900900	-0.00057300
O	-1.86083700	2.79221000	-0.00025500
Na	4.53978900	-1.76915700	-0.00026700
H	1.47127200	-2.06719200	-0.00017600
H	4.62629200	1.32009600	0.00153300

Coordinates of the optimized structures of lowest energy conformer of sodiated anthrarufin at B3LYP level with the basis set 6-311++G(d, p)

1	1		
C	3.13910	0.17642	-0.00018
C	3.79908	-1.06659	-0.00058
C	3.07242	-2.23887	-0.00057
C	1.67357	-2.21898	-0.00018
C	1.00180	-1.00474	0.00006
C	1.72627	0.20874	0.00009
C	1.03745	1.48434	0.00042
C	-0.45340	1.48889	0.00023
C	-1.19091	0.28033	0.00015
C	-0.47196	-1.00910	0.00050
C	-2.59645	0.38736	-0.00040
C	-3.21559	1.63417	-0.00086
C	-2.46611	2.79906	-0.00033
C	-1.07957	2.72701	0.00018
H	-0.46429	3.61843	0.00044
H	-2.96725	3.76044	-0.00034
H	-4.30183	1.69161	-0.00134
O	1.64936	2.55492	0.00073
H	1.10688	-3.14096	-0.00009
H	3.59467	-3.18941	-0.00082
H	4.88314	-1.06908	-0.00082
O	3.87909	1.27273	-0.00016
O	-1.07841	-2.08780	0.00107
Na	-2.99633	-3.02717	0.00012
H	3.26741	2.04809	0.00011
O	-3.41166	-0.72800	-0.00030
H	-4.32046	-0.40337	-0.00043

Coordinates of the optimized structures of lowest energy conformer of sodiated chryzarin at B3LYP level with the basis set 6-311++G(d, p)

1	1		
C	2.40785	-1.24640	-0.00293
C	3.73418	-0.78937	-0.00339
C	4.00333	0.56221	-0.00153
C	2.96211	1.49968	0.00077
C	1.65126	1.06842	0.00089
C	1.33410	-0.31423	-0.00109
C	-0.03791	-0.77474	-0.00049
C	-1.14138	0.20339	-0.00140
C	-0.84028	1.58734	0.00147
C	0.57254	2.07983	0.00368
C	-1.83478	2.55407	0.00136
C	-3.16956	2.17516	-0.00182
C	-3.49744	0.82969	-0.00465
C	-2.50779	-0.14850	-0.00433
O	-2.92869	-1.46614	-0.00739
H	-4.54303	0.52939	-0.00699
H	-3.95603	2.92134	-0.00205
H	-1.53768	3.59588	0.00358
O	-0.27852	-2.01356	0.00082
H	3.16060	2.56469	0.00257
H	5.03314	0.90280	-0.00176
H	4.52649	-1.52892	-0.00507
O	2.21669	-2.56249	-0.00449
O	0.80779	3.27044	0.00721
H	-3.89345	-1.44302	-0.01470
Na	-1.85366	-3.49024	0.01267
H	1.24473	-2.69492	-0.00347

Coordinates of the optimized structures of lowest energy conformer of lithiated alizarin at B3LYP level with the basis set 6-311++G(d, p)

1	1		
C	-2.15458	-0.60959	0.00001
C	-3.18276	0.34269	0.00047
C	-2.89146	1.69613	0.00053
C	-1.56378	2.10323	0.00002
C	-0.53511	1.17235	-0.00025
C	-0.81103	-0.21547	-0.00024
C	0.29995	-1.18548	-0.00054
C	1.67814	-0.69210	-0.00002
C	1.95924	0.68632	-0.00012
C	0.86493	1.68651	-0.00055
C	3.27973	1.12423	0.00022
C	4.31883	0.20018	0.00072
C	4.04487	-1.16763	0.00086
C	2.73191	-1.61392	0.00045
H	2.50649	-2.67331	0.00053
H	4.85895	-1.88383	0.00128
H	5.34690	0.54588	0.00100
H	3.47217	2.19105	0.00009
O	0.08397	-2.41093	-0.00121
H	-1.30394	3.15537	-0.00005
H	-3.69421	2.42718	0.00098
O	-4.42703	-0.19995	0.00128
O	-2.56553	-1.92584	-0.00005
O	1.08793	2.87959	-0.00105
H	-5.12246	0.46587	-0.00248
H	-3.53900	-1.90765	0.00055
Li	-1.39762	-3.40946	-0.00101

Coordinates of the optimized structures of lowest energy conformer of lithiated anthrarufin at B3LYP level with the basis set 6-311++G(d, p)

1	1		
C	2.76186	0.39260	0.00002
C	3.63511	-0.68746	0.00001
C	3.14579	-1.98472	-0.00003
C	1.77497	-2.20801	-0.00006
C	0.89939	-1.13185	0.00001
C	1.36614	0.20391	0.00009
C	0.39660	1.31299	0.00005
C	-1.03743	1.01123	-0.00004
C	-1.49565	-0.32745	-0.00001
C	-0.56066	-1.43520	-0.00000
C	-2.88411	-0.58469	0.00000
C	-3.78560	0.49825	0.00001
C	-3.31715	1.79510	-0.00003
C	-1.94400	2.06350	-0.00005
H	-4.02358	2.61785	-0.00003
O	0.77273	2.49997	0.00006
H	1.36364	-3.21016	-0.00014
H	3.83832	-2.81882	-0.00002
H	4.70844	-0.51324	0.00004
O	3.31423	1.66589	-0.00000
O	-0.93760	-2.60841	-0.00002
H	4.27496	1.57230	0.00024
O	-3.38631	-1.80696	0.00004
H	-2.63300	-2.44479	0.00006
H	-1.57915	3.08248	-0.00007
H	-4.84701	0.27731	0.00006
Li	2.35382	3.30798	-0.00020

Coordinates of the optimized structures of lowest energy conformer of lithiated chryzarin at B3LYP level with the basis set 6-311++G(d, p)

1	1		
C	-2.50633	1.06845	-0.00042
C	-3.73524	0.38932	-0.00246
C	-3.76828	-0.98708	-0.00294
C	-2.58093	-1.73480	-0.00139
C	-1.36370	-1.08853	0.00031
C	-1.28788	0.33082	0.00066
C	-0.01883	1.00849	0.00205
C	1.23446	0.23592	0.00056
C	1.17960	-1.17802	0.00116
C	-0.12881	-1.90352	0.00223
C	2.32976	-1.95336	0.00036
C	3.57741	-1.34505	-0.00136
C	3.66638	0.03822	-0.00229
C	2.51813	0.81873	-0.00134
O	2.68880	2.19761	-0.00261
H	4.64215	0.51845	-0.00362
H	4.48241	-1.94188	-0.00200
H	2.22223	-3.03150	0.00097
O	0.01185	2.27783	0.00363
H	-2.59731	-2.81810	-0.00140
H	-4.72447	-1.49914	-0.00446
H	-4.64224	0.98259	-0.00350
O	-2.55127	2.39451	0.00023
O	-0.15746	-3.11613	0.00294
H	-1.62656	2.71437	0.00198
H	3.63696	2.37776	-0.00761